Masters
Program
in **Geospatial**
Technologies

AUTOMATIC VISION BASED FAULT DETECTION ON ELECTRICITY TRANSMISSION COMPONENTS USING VERY HIGH-RESOLUTION IMAGERY AND DEEP LEARNING MODEL

Chukwuemeka Fortune Igwe

Dissertation submitted in partial fulfilment of the requirements
for the Degree of *Master of Science in Geospatial Technologies*

NOVA IMS Information Management School

Universitat Jaume·I

Westfälische Wilhelms-Universität Münster

Automatic Vision-Based Fault Detection on Electricity Transmission Components Using Very High-Resolution Imagery and Deep Learning Model

Dissertation supervised by
Joel Dinis Baptista Ferreira da Silva, PhD
NOVA Information Management School ()
Universidade Nova de Lisboa (UNL)
Lisbon, Portugal

and co-supervised by
Prof. Edzer Pebesma, PhD
Institute for Geoinformatics (IFG)
University of Münster
Heisenbergstr. 2, D-48149 Münster.

Ditsuhi Iskandaryan
GEOTEC
Universitat Jaume I
Castelló, Spain.

February 2021

Declaration of Originality

I declare that the work described in this document is my own and not from someone else. All the assistance I have received from other people is duly acknowledged, and all the sources (published or not published) are referenced.

This work has not been previously evaluated or submitted to NOVA Information Management School or elsewhere.

Lisbon, February 16, 2021.

Chukwuemeka Fortune Igwe

[the signed original has been archived by the NOVA IMS services]

Acknowledgments

The acknowledgment of this project is split seven ways:

To the *Triune*, who gave light during my darkest days and made me whole during the times when all things were against me; for their continuous reproof, guidance, sustenance, and coordinated directions.

To my well-disposed supervisor, **Dr. Joel Silva,** for taking the time to go over this thesis for correction meticulously and his valuable suggestions. His blitheness knows no bounds as that at every unceasing demand made by me; he offered conscientious criticism and invaluable guidance to the thesis progress even with a busy schedule.

To *my co-supervisors*, **Prof. Dr. Edzer Pebesma** and **Ditsuhi Iskandaryan** (Ph.D. in view), for their guidance, technical and constructive criticism on the thesis dissertation. Also, to *my Course Coordinator, **Prof Marco Painho***, for sharing his experience and giving his time and effort in giving moral support throughout; for his patience during times, we commit failure and gross errors, and big thanks for motivating me to work harder.

To my mentor, **Prof. F. I. Okeke** and **Dr. Iyke Maduako** helped me acquire the necessary data and trusted enough to accomplish this thesis. Also, I am grateful to the Sterblue team and Geogeek group, who served as a guide to becoming knowledgeable with deep learning concepts and power industry Jargons.

To *my parents, **Mr. & Mrs. A. C. Igwe,** and my siblings, **Zainab, Stanley, Aminu, Kasie,*** for their understanding, support, unfailing advice, words of encouragement, and prayers during this period. I indebted to them for their undying love and support; for always being there for me; for making me feel how much they are proud of me; for their teachings and guidance, which made me become what I am now. Without them, I would never have gotten a strong formation and had the sense to soar higher. You all remain my inspiration, strength, and motivation to fulfill my dreams and accomplish this phase.

To my newfound family, *my colleague and course mate **"Geotech class of '21"***, for their enchanting company, challenge, friendship, and encouragement in hard times and during this thesis dissertation. I want to thank Erasmus Mundus for supplying me with the resources required to achieve this astounding master's degree.

To *my relatives, **the Isiofias**,* most especially Mr. Chukwuemeka Isiofia, for their support during this journey towards achieving my Masters. Finally, **to you**, who contributed in diverse ways towards completing my study, and if you have stuck with me until this very end.

Automatic Vision-Based Fault Detection on Electricity Transmission Network Components Using Very High-Resolution Imagery and Deep Learning Model

Abstract

Electricity is indispensable to modern-day governments and citizenry's day-to-day operations. Fault identification is one of the most significant bottlenecks faced by Electricity transmission and distribution utilities in developing countries to deliver credible services to customers and ensure proper asset audit and management for network optimization and load forecasting. This is due to data scarcity, asset inaccessibility and insecurity, ground-surveys complexity, untimeliness, and general human cost. In this context, we exploit the use of oblique drone imagery with a high spatial resolution to monitor four major Electric power transmission network (EPTN) components condition through a fine-tuned deep learning approach, i.e., Convolutional Neural Networks (CNNs). This study explored the capability of the Single Shot Multibox Detector (SSD), a one-stage object detection model on the electric transmission power line imagery to localize, classify and inspect faults present. The components fault considered include the *broken insulator plate*, *missing insulator plate*, *missing knob*, and *rusty clamp*. The adopted network used a CNN based on a multiscale layer feature pyramid network (FPN) using aerial image patches and ground truth to localise and detect faults via a one-phase procedure. The SSD Rest50 architecture variation performed the best with a mean Average Precision of 89.61%. All the developed SSD based models achieve a high precision rate and low recall rate in detecting the faulty components, thus achieving acceptable balance levels F_1-score and representation. Finally, comparable to other works of literature within this same domain, deep-learning will boost timeliness of EPTN inspection and their component fault mapping in the long - run if these deep learning architectures are widely understood, adequate training samples exist to represent multiple fault characteristics; and the effects of augmenting available datasets, balancing intra-class heterogeneity, and small-scale datasets are clearly understood.

Keywords

Single Shot Multibox Detector (SSD)

Convolutional Neural Network

Deep Learning

Unmanned Arial Vehicle Imagery

Electric Power Transmission Network Components

List of Acronyms and Abbreviations

CNN - Convolution Neural Network

DCNN - Deep Convolution Neural Network

DDN - Defect Detector Network

DEM - Digital Elevation Model

DL - Deep Learning

ELU - Exponential Linear Unit

EPTN - Electric Power Transmission Network

ESA - European Space Agency

ETL - Electric Transmission Lines

FPISA - Faster Pixel-wise Image Saliency Aggregating

Faster RCNN - Faster Region-based Convolution Neural Network

GSS - Graphical Shed Spacing

GSO - Graphical Shed Overhang

HSV - Hue Saturation Value

ILN - Insulator Localizer Network

LIDAR - Light Detection and Ranging

MLP - Multilayer Perceptron

NMS - Non-Maximum Suppression

R-FCN - Region-based Fully Convolution Network

RADAR - Radio Detection and Ranging

ReLU - Rectified Linear Unit

ResNet - Residual Network

RGB - Red Green Blue

RoI - Region of Interest

RUE - RoI Union Extraction

S-AM - Saliency and Adaptive Morphology

SAR - Synthetic Aperture RADAR

SSD - Single Shot Multibox Detector

SVM - Support Vector Machine

TCN - Transmission Company of Nigeria

UAV - Unmanned Aerial Vehicle

VGG - Visual Geometry

VHRI - Very-High Resolution Imagery

Index of the Text

Index of Tables

Index of Figures

1 Introduction

1.1 Contextual Background

Growing population and a shortage of energy availability have placed problems for economies concerning the development of effective manufacturing industry, citizens' expectations, and livelihood sustainability. According to the United Nations (UN), electricity, among others, is a necessity for life [1]. The UN Sustainable Development Goals 7 for 2030 has specifically established one of their key priorities: improving equitable access to cost-effective, secured, and optimum energy (electricity) resources [2]. This can be done by expanding infrastructure and updating technologies to deliver sufficient energy facilities via consistent energy efficiency monitoring, particularly for developed countries. Accordingly, remote sensing techniques have proven to be an efficient tool in which defects such as corrosion and mechanical loss can be managed and identified, power component damage detected, and energy supply conditions monitored, especially with UAV surveillance [3]. As a result, various public-private partnerships (PPP) are being established to tackle and upgrade existing systems. One of the challenges for these PPPs is the current dilapidated state of most power transmission assets and infrastructure [4], [5]. Other challenges they face include meeting customer demands; forecast and distribution of customer's load; excessive cost; customer service delivery; capturing of accurate, up-to-date information of network infrastructures and asset; network optimization; cybersecurity; fault resolution and outage; and technical and commercial losses [4]–[7].

In terms of faults in electrical transmission and control systems, defects such as breakage and corrosion are a significant source of in-service system deterioration and disruption [8]. Once faults are not handled at their early stages, it may soon affect system reliability, resulting in the drop in voltage, network diminishment, grid destruction, along with increasing outages, with ultimately impact threatening repercussions to the ecosystem [9]. This ultimately has unintended consequences in the form of cost and sanctions. This was further emphasized by an annual report released in the US, which evaluates the corrosion cost at about $276 billion in maintenance [10]. In other climes like Brazil, the 2010 large-scale blackout that impacted 11 of the 27 states containing 6 million people was attributed to corrosion and wear of transmission lines [10].

Before integrating the IT system in early 2010 [4], [6], manual methods were conventionally employed by the electricity distribution company. Electrical linesmen were sent to the site to inspect, track, and maintain distribution and overhead power lines with mechanical devices. This procedure generally included pole climbing, foot patrols, and vehicle inspection, involving just human subjectivity [3]. These manual methods are time-consuming, labour-intensive, imprecise, and risky. Providentially, the current availability of fast computers, digital data acquisition technology, digital data processing technique, information technology, and geographic Information system brought a revolution into electricity distribution [4]–[7]. For example, in fault analysis, network optimization, asset audit, load forecasting, customer indexing, and listing [4]–[7], GIS and GPS have been used to provide database management capabilities and pinpoint the location of electrical assets. However, this process is cumbersome and exposes utility staff directly to unsafe conditions during inspection [3].

As a result of these, other geospatial technique has been adopted. Most notable is the use of very high-resolution imagery (VHRI) via Unmanned Aerial Vehicle (UAV) surveillance using red-green-blue (RGB), light detection and ranging (LIDAR), radio detection and ranging (RADAR) [12], or a modular combination of any of these sensors [3], [11]. UAV monitoring offers high-spatial multispectral images that deal with the limitation of other techniques with the benefit that they can capture accurate images of transmissions components at closer proximity [13], which are very useful for the detection of small-scale defects such as broken fittings and missing knobs and can be incorporated with other modes of remote sensing.

Most research only considers the transmission lines' delineation after the data has been captured using different mathematical models. However, to create an automated vision-based fault detection system for power transmission networks utilizing high-quality remote sensing imagery [13], a high-level vision task is needed to adopt a high-level vision task capable of advanced learning characteristics and generalization. Currently, improved algorithms and multilayer neuron systems such as CNN, DNN, and RNN have demonstrated more outstanding performance than standard approaches, particularly in power line identification, transmission components detection, and vegetation encroachment prevention [14]. The traditional approach for pattern recognition depends on the parameters that are well built by humans. Hence, this manual extraction process is inefficient, unfavourable, and inadequate for generalization necessities.

Also, most machine learning approaches using primary neural networks need vast quantities of standardized hand-made structured training data in the form of rows of records, which can be cumbersome. With deep learning algorithms, visual perception to extract feature hierarchies and generalization ability is enhanced on several levels [15]. These algorithms have demonstrated that conventional learning methods are sluggish and unreliable; they require substantial post-processing attempts to differentiate between transmission infrastructure [16]. Succinctly, power transmission network mapping and defect inspection require a more advanced adequate hybrid classifier that is way beyond task-based approaches, promoting the improved performance of visual recognition tasks and successfully adapts from multimodal data sensors for object detection.

Therefore, by leveraging VHRI and robust classifiers with deep learning models, the PPPs can ensure comprehensive and accurate track of the conditions, especially corrosion of their transmission line assets wherever they are, both as part of service provision, network expansion, and routine maintenance. Additionally, for many electricity companies, especially private electricity distribution Companies: a critical step in ensuring smooth service delivery lies in monitoring the electricity distribution assets [4], [7]. Hence, they must know what assets they have, where they are, their state, and how they are working.

1.2 Problem Statement and Motivation

In traditional operations, utilities must power off entire distribution grid sections to identify damaged outgoing lines. Many power grids are linked across the network. A domino effect in one field can also lead to supra-regional blackouts [11]. After finding the damaged line, technicians will power the faulty line part by part until they ultimately locate the ground fault. This process often takes several hours or even days, further made strenuous by unfavourable weather conditions and mountainous terrain. Usually, field and airborne surveys that are quite challenging are standard methodologies used for decades for inspecting power networks [3], [11]. However, this traditional approach is limited in terms of accuracy and ability to extract features at multiscale as well as portrays a low-level generalization ability. In recent years, several studies have been undertaken to automate the inspection of defects using remote sensing satellite and aerial images, including LIDAR, SAR, and optical images; however, very little public analysis and implementation have been adopted and published. They focus mainly on mapping and monitoring the power line components and vegetation invasion encroachment adjoining transmission lines. These studies are generally carried out majorly in developed countries like China, where adequate data with high quality are easily acquired by qualified technical know-how propelled by the right motivation and adequate funds. Alternatively, developing countries such as Nigeria are limited to such very high multispectral data needed for a complete overhaul of transmission assets.

Nigeria's development agenda is anchored in a vision that identifies energy as one of the vital infrastructural enablers for development. For a country to successively make a significant positive transition in development, it must have efficient, reliable, vast, and environment-friendly energy source transmission. This power should also be availed at the points of demands consistently and effectively. This means that majority of the burden of energy demand is on power companies to provide and transmit quality energy services to consumers. Against this backdrop, the recent images available inspire research and development in maintenance and asset inventory to overcome such difficulty and look for effective and sustainable solutions. Based on that, deep learning has demonstrated potential promising advances in power line component inspection and other study fields. Thus, the potential solution of developing an automatic vision-based fault detection system that uses multispectral images and deep learning (DL) framework also adds motivation to conduct this study.

1.3 Research Aims and Objectives

This research seeks to detect and inspect vision-based components' faults on the electricity transmission line using very high-resolution UAV imageries (VHRI) and deep learning techniques (DLT). To achieve these main research aims, the following sub-questions are addressed:

a) Which different hyperparameters finetuning yields the best results in the implemented deep learning model?
b) To what extent will the deep convolution neural network perform based on the predicted component fault classes' performance metrics analysis?

1.4 Contribution

Most current studies focus separately on either identifying transmission assets or detecting a single fault on transmission components individually using either traditional methods or DL. However, this research focuses on the following contributions:

- → Explore the feasibility of using a single-phase deep learning model and affordable drone surveillance to develop a power line component fault detection and classification pipeline for a series of faults (multi-class) that typically exists on power transmission components. Based on my understanding, very little research has been carried out here as most implemented or underway are proprietary and have provided little benefit to the research communities and electric utilities.
- → Empirically, evaluate via comparative analysis different backbone architectures to classify and localize multi-class electric power transmission component fault.

1.5 Thesis Organization

This thesis is divided into seven chapters. The remainder of this thesis is organized as follows. Chapter 2 reviews vision-based inspection in the electric power transmission network (EPTN). It further evaluates the related works on the existing approach and technique utilized for electric transmission components fault detection. Chapter 3 provides a theoretical background needed to understand the basic concept approaches applied to the thesis methodology. Deeper explanations are given on the convolution neural networks (CNNs) basic building blocks concept and image classification that serves as backbone architecture for feature extraction. In addition, a brief exposition of the SSD as the meta-architecture of choice is presented. Chapter 4 outlines the research location and describes the dataset used in the potential deep learning models. It further describes the research problem, i.e., how each components' faults appear. Chapter 5 describes extensively the method adopted in this work. It provides details about the data pre-processing, network training of the deep learning framework, and the hyperparameter augmentation and validation approach.

Furthermore, the evaluation and performance metrics utilized are established. In Chapter 6, the evaluation and comparison of hyperparameter configurations and results over the three implemented SSD-based models were discussed via outline, graphs, and overview. It aims to show fusing deep learning and high-resolution RGB oblique imagery; it is feasible to build a model that better identifies component fault of interest in cluttered backgrounds. The thesis concludes by summarizing the findings and possible directions of the analysis for future works in Chapter 7.

2 Literature Review

2.1 Vision-Based Inspection and Faults Diagnosis in Electricity Distribution

The inspection of electric transmission lines (ETL) has become an essential concern because virtually all human communities, processes, and mechanisms rely on electricity. External forces, especially meteorological influences, have been identified as the primary cause of the collapse of electric power transmission networks (EPTN) [18], [20]. Hence, frequent monitoring and assessment of the transmission line are necessary to strengthen and sustain the transmission network and provide reliable and quality service delivery to customers [5].

According to Chen et al. [21], faults associated with electrical power grids are described as accidental short circuits, or a prolonged short circuit, between power-conductors or an energy-efficient conductor and the ground due to wear, corrosions, and interruptions by adjoining ecosystem, causing irregular electrical current. Generally, ETL faults are classified into symmetrical (balanced) and unsymmetrical (unbalanced). In engineering, a fault is symmetric if it impacts all phases equally (three lines), while it is unsymmetric when it does not affect each of the phases equally [18], [23]. Nonetheless, many power system failures are fundamentally unsymmetrical. This is because the current induces unevenness. This implies an unequal difference in the frequency of fault currents along the usual three-phase conductor (wires) present in the ETL [18].

The electricity line inspection aims to verify these faults on a power line, the output of which is used as a reference to determine which components to retain or replace. A precise and straightforward inspection will make sustaining decisions more effective and reduce the risk that the transmission network will fail, facilitating secure and stable power distribution [3], [19]. Overhead power line inspection by a human observer and airborne surveys is the most utilized means for regular inspection and power line maintenance. With the increased advancement of technologies, geo-referenced remote sensing techniques such as the Unmanned Aerial Vehicle (UAV) mounted with different sensors have become a great alternative providing rich data sources for data analysis.

The UAV is operated manually or automatically along the power lines corridors. Multiple sensors are used on the aircraft to track and gather data during this operation. A variety of benefits of the UAV make it a preferred inspection method: 1) Proximity to problematic areas, which allows data collection incredibly versatile, 2) Ability to load multiple inspections sensing instruments, 3) Fix low-efficiency issues and line harm, 4) saves time and human resources and is associated with a high rate of safety. With this technology, data processing is distinguished from data acquisition using digital data captured via remote sensing sensors and laser scanners. This is especially relevant as data acquisition practices now concentrate solely on cost-reduction; hence, allowing precise assessment, repeated study, and persistent data storage enabling multi-temporal analysis and evaluation [3].

The UAV images serve as an inexhaustible source of information for utilities to know where assets are located, their functional status, and to determine their net worth. This falls into a broader system that assists with a well-organized inventory of distribution facilities for optimum electric lines, pole support infrastructures, transformers, and all network assets fault diagnosis [3]. Combining these data with scientific and technological developments like artificial intelligence enables an ever-increasing volume of data to be processed and has increased growing research on the use of UAV survey imageries to allow the conditions on power lines to be distinguished automatically [24]. In the classification of the insulator status, Zhao et al. [25] have proposed object detectors and insulator fault detection processes utilizing multi-patch in-depth features learnt from the aerial images to classify the insulator into normal, damaged, dusty, and missing caps.

2.2 Remote Sensing in Power Line Inspection

To investigate the electric power transmission network (EPTN) usually located in remote areas, various data sources ranging from coarse-resolution satellite images to detailed ground images and point clouds obtained via ground vehicles are utilized. These data sources primarily result from optical, microwave, and LIDAR (LASER) remote sensing techniques. These approaches provide multispectral imagery with varying temporal resolution access based on operational capabilities and technical limitations [11]. Studies presented using microwave sensing imageries, majorly employ synthetic aperture radar (SAR), have noted the advantage of being acquired in all weather conditions, making them particularly interesting to inspect powerlines, most especially during disaster monitoring [27].

For example, Xue et al. [27] utilized SAR image-based systems for landslide detection to measure electricity towers’ damage. Based on pixel resolution, morphology algorithm, and location of the damage caused by landslides, the authors detected and geotagged power lines damaged by landslides directly. The use of TerraSAR-X imagery of high-resolution in spotlight mode with 300 MHZ range bandwidth to track power line towers in natural disaster situations was discussed by Yan et al. [28]. SAR imagery was preferred to optical imagery as the author points out that SAR geometry makes it suitable to detect vertical, human-made objects, such as power towers. The critical theory was that towers were finally derived from single imagery, and the estimated tower height information was used to detect fallen or deformed towers.

Sentinel-1 SAR satellite from the European Space Agency, ESA, and other very high-resolution (VHR) SAR images (TerraSAR, RADARSAR) that are higher than five metres have recently opened a wide range of surveillance, tracking, and monitoring of power transmission systems [29]. However, VHR SAR for EPTN seems impacted by distortions connected to imagery, the particularly pseudo-random variation of the different components imprints, making it semantically challenging to interpret [30]. They are also limited by coarse resolution to detect small defects in electricity transmission components, geometric deformations, strong noise-like effect creating false representations, and multi-path scattering [11], [27]. In light of this, various studies of transmission line inspections utilize multispectral images acquired from optical satellite remote sensing, as it allows for straightforward interpretation. However, these data are still restricted by resolution in power line inspections.

Optical remote sensing has focused on fault diagnosis for the different EPTN components themselves because the ground sample distance (GSD) is usually greater than the individual components' size, especially for those caused by the adjoining environment. As a result, most power line inspection research is fixated on vegetation encroachment and minimum height and clearance distance [14], [31]. Additionally, a stereo pair of optical satellite images have been utilized to extract the canopy height model to monitor damages to EPTN caused by vegetation [32]. This has allowed the identification of individual overgrown trees affecting power lines with high accuracy. The studies on vegetation encroachment faults affecting transmission lines from satellite and aerial images have habitually utilized the classification of trees, extraction, vegetation indices, and segmentation approach. Vegetation invasion on transmission lines was studied by Ahmad et al. [31]. The paper explored the use of multispectral satellite stereo imagery to simulate transmission lines using a 3D digital elevation model (DEM) to detect dangerous vegetation branches that could affect power lines and cause blackouts.

Apart from vegetation encroachment, a variety of papers addressed automatic inspection of insulators' condition. These techniques aimed to take images of the insulators periodically and use automated classification methods to identify damaged insulators. Reddy et al. [33], for example, used fixed cameras on poles. Jiang et al. [34], using a photogrammetric method, addressed flashover faults - pollution-related flashes affecting insulators. In the experiment, a sensing camera placed on a tripod was used. However, most remote optical sensing techniques are primarily restricted by the atmosphere. Consequently, using the Lidar method through airborne laser scanning or mobile laser scanning has also been used to improve the shortcomings of multispectral optical images to detect and identify tall trees that may collapse through the conductor and exceed the required vegetation clearance. In responsive inspections and audits for transmission lines, such as catenary modelling for thermal upgrade and vegetation encroachment research, Ussyshkin et al. [35] explored using LIDAR data.

Other remote sensing techniques have further involved integrated sensors, which majorly involves integrating ultraviolet images over both an infrared and multispectral visible colour image. For instance, a UAV surveillance incorporated with optical and thermal Infrared sensors was identified by Luque Vega et al. [36] for the power transmission network. The corona impact can be located by utilizing the different layers' stack, and the ultraviolet/infrared image can be analysed for damage and phenomenon magnitude [11]. The most exciting uses for satellite data concerning power lines have been automatic extraction of power transmission components [11], power lines affected by vegetation encroachment [17], damaged transmission tower [27], and damaged conductor faults at a coarse level over large areas [26]. It is possible to apply optical and SAR images. Airborne and terrestrial scanning systems have more reliable information than satellite imagery, but it is impossible to regularly cover vast regions. Optical images captured by UAVs are proposed as a data source since (i) they are easily accessible and available, and (ii) they can be analysed very quickly, while (iii) ample information is given for the identification of a wide variety of common small defects in both power components and power lines. Most literature has yet to address more than one fault affecting the power line and detect small faults.

2.3 Traditional Approach for Power Transmission Lines Fault Detection

Optical imagery, particularly multispectral RGB images, has proven to be effective means for automatic inspection and identification of power transmission lines components compared to traditional ground-based surveys, which consume a lot of money, time, and human resources [37]. Hence, making it a better choice of detecting and classifying faults critically across electricity networks. In terms of fault detection approaches, they can be grouped into two types in general: supervised and unsupervised classification [38], [39]. Many methods for the automated identification and monitoring of the electric power transmission network (EPTN) faults have been implemented in recent years using supervised classification.

The typical detection process can be divided into two stages: extraction of feature and feature (fault) classification [24]. Features are extracted from images and subsequently inserted into the classifier to identify the components' faults. Significant parameters for these features (ETPN components) classifications, which are primarily used, include colour, form, texture, and fusion. A widely used approach applied to check faults of power line components primarily involves clustering, mathematical-based techniques such as Hough transform, Gabon filters, and low-level filters. In detecting broken transmission line spacers, a Canny edge detector combined with Hough transform [40] by Song et al. extracts the conductors. First, a scan window was formed in the path of the conductor. During the convolution process, if there are a candidate's spacers, they are recognized in all sliding windows. Finally, the shape configuration parameter was structured to decide whether the sensed spacer was broken based on the measurement of linked parts. However, several factors can make it challenging to extract power line components' faults automatically. These include complex background, camera viewing angle at the moment of capture, background light and spectral resonance, weather, and seasonal changes in the background [3], [11].

The icing status of insulators was measured by Hao et al. [41] on the basis of the iced insulator geometric framework. The knowledge-based rules were designed to define the glaciation state by the distance between two neighbouring insulator caps using Graphical Shed Spacing (GSS) and Graphical Shed Overhang (GSO). Similarly, an improved uniform LBP (IULBP) was proposed for feature extraction of thaw insulator using the texture variable difference between predefined ice template type and the feature extracted from IULBP Yang et al. [42]. Zhai et al. [43] exploited Saliency Aggregating Faster Pixel-wise Image (FPISA) for insulator extraction. Based on the colour channel in Lab colour space, the observed insulator's flashover region was extracted. The system was tested using 100 flashover fault insulating images and obtained a detection rate of 92.7%. Zhai et al. [44] and Han et al. [45] detected the faults associated with missing-cap of insulators based on saliency and adaptive morphology (S-AM).

One of the most challenging fault diagnosis tasks is faults with a tiny aspect ratio on the EPTN components, for instance, power line fitting such as missing pin, nut, bolts, and a small degree of fault severity on some large components. To detect such kinds of faults, aerial images are captured close to the exact components containing the faults or the components (or faults) cropped from the original image manually [46], automatically, or via segmentation [47]. Fu et al. [48] implemented a dynamic model for the missing pin type of faults. The fitting is usually a combination of multiple sections, such as pin and nut, for example. The haar-like attribute and Adaboost classifier was used to detect each part of the fitting. The methodology involved first extracting the segmented region and circles with LSD. and Hough transform, respectively, to identify the missing pin. The missing pin fault was finally obtained and then observed based on the distance limit between the centre of the circle and the pin section. This procedure was validated using 42 images. Out of the five images with pin fitting identified, only one of them was classified correctly.

In terms of conventional classification, machine learning-based algorithms have also been used as the feature classifier, primarily Adaboost [48], SVM [49], which have been applied successfully to detect foreign bodies on conductor faults. Most literature has dealt with majorly components detection over the years compared with fault detection associated with these components. Essentially, a fault has different types and affects different components, requiring robust architecture to tackle the problem. Overall, most faults detected focused on the missing insulator head, while other EPTN fault types are limited. Study on the other components continues to dwindle because of variations of components, inadequate data, and inappropriate scale. Furthermore, in most cases, each research study is centred only on one fault of a particular component. Hence, the deep learning concept is proposed to handle some of these limitations that have been stated above.

2.4 Deep Learning Algorithms for Power Transmission Lines Fault Detection

Prior studies have employed the deep learning approach to multispectral images (RGB channel) for fault detection. Most of them have achieved better performance than the study using knowledge-based or physical parameters as described above. The articles [46], [47], [50], [51] contain comparative studies for a single type of fault. The most notable deep learning models have been developed for EPTN faults with several essential considerations in mind due to the need for robustness and generalization capability. These considerations include data augmentation, data resizing to deal with small aspect ratio, and high-resolution images collected from UAV. Data augmentation is usually adopted to overcome data insufficiency, add variability, and increase the robustness in research [47], [50], [52], [53]. DL is a deep convolution neural network (DCNN), which offers a hierarchical representation of knowledge that facilitates a greater understanding of problems' complexities [16]. Promising DL approaches used to detect faults through EPTN components are addressed in this section.

Deep learning-based object detection consists of two components: a DCNN for the feature extraction model (also referred to as a backbone) and the object classification and localization scheme (meta-architecture) for the project [54]. According to the detection system, the DL-based detection process is classified into two categories: the two-stage and the one-stage detection approach [54]. The former consists of an additional stage for region proposal network formation and abstracting the region of interest (object) such as Faster RCNN [55] and R-FCN [56]. The latter stage does not require proposals network generation. The one-stage detection approach, for instance, SSD [57], eliminates the protocol for proposal generation and reduces processing operations, storage requirement, time, and computing capacities.

One of the earliest works on fault detection was detecting surface discoloration due to flashover on insulator using CNN classifier with pre-trained AlexNet published by Zhao et al. [25]. The experiments were performed with a score of 98.71% mAP on 1000 samples. Faster R-CNN was applied by Liu et al. [53] to identify insulators with missing caps. The system was tested for three different voltage transmission line levels with 1,000 training samples and 500 research samples prepared for each level. About 120 photographs (80 for training) were used to test the diagnosis of missing cap fault. The entire experiment was carried out by resizing all images to 500 x 500 pixels and flipping and cropping to expand the dataset. Similarly, Jiang et al. [58] developed a novel approach using SSD as the meta-architecture for multi-level perception (low, mid, and high perception) based on ensemble learning to extract the missing insulator fault from the image resolution of 1920 × 1080-pixel. The middle and high-level perception images are made via the ROIs Union Extraction (RUE) image pre-processing. The proposed approach's absolute precision and recall rates were 93.69% and 91.23% on the test image dataset with various perception levels containing missing cap insulator problems. However, these papers considered the contextual characteristics of one type of fault that affect the insulator component.

One particular issue in power line fault detection using deep learning CNN is data insufficiency. This is because the DL model is required to generalize the solution at the end of the training. To achieve this, a robust and large amount of dataset is usually required. In the previous papers to tackle this challenge, attempts were made, such as synthesized images (e.g. [59]) and data augmentation (e.g., [52], [53]). Other researchers have examined the use of transfer learning and few-shot learning to identify fault types. The model was first developed using the ImageNet data kit, which included a 1.2 million samples dataset. This same model was then trained, i.e., fine-tuned by the limited data set obtained containing the surface fault of insulators by Bai et al. [60] based on the SPP networks (SPP-Net) with transfer learning approaches. This allowed the weight optimization to begin at top layers (where there is a different feature complexity from the original training data utilized) in the 3D CNN of the SPP-Net adopted rather than for the whole model.

In recent years, there have been few efforts to develop the deep learning approach, which has made it ideally suited for identifying power lines faults. Typically, a two-step object detection technique is commonly utilized: first, to identify the component and second, to detect the fault in those components. In this light, Tao et al. [59] developed two separate backbone models, D.D.N. and I.L.N. (V.G.G. and ResNet, respectively), based on domain knowledge of EPTN components structure. In order to find a missing cap fault, a cascading architecture combining a custom-developed Insulator localizer Network (ILN) and a Defect Detector Network (DDN) models were utilized. The ILN identifies all the insulators in the aerial image and then cuts the detected areas and feeds them into the DDN. A total of 900 regular images were collected from UAV for this experiment and 60 defective images. Data insufficiency was tackled by segmenting the image using the U-net algorithm to divide the output of the ILN into insulator and background. The segmented insulator was then combined with distinct images of different backgrounds to mimic real-life background situations concerning insulator position. The result of this was then merged as input for the DDN development. Finally, about 1956 pictures for ILN (1186 for training) and 1056 images with missing caps (782 for training) were prepared. The DDN detection precision and recall are 0.91and 0.96.

3 Theoretical Background

3.1 Convolutional Neural Network

Convolutional neural networks (CNNs) are an ensemble of artificial neural networks designed to recognize and identify objects or images on the basis of their ability to learn spatial, topological, and contextual representations and patterns resulting from internal activations, usually an input image [24]. The CNN architecture consists of the input layer, the hidden layer, and the output layer, similar to the multilayer perceptron (MLP). The input and output layers are known and describe the input image dataset and its corresponding class label annotation (or associated prediction). The hidden layer(s) is the most important, denoting the layer depth is mainly divided into three layers: Convolutional, Pooling, and Fully Connected, also known as Dense Layer [61].

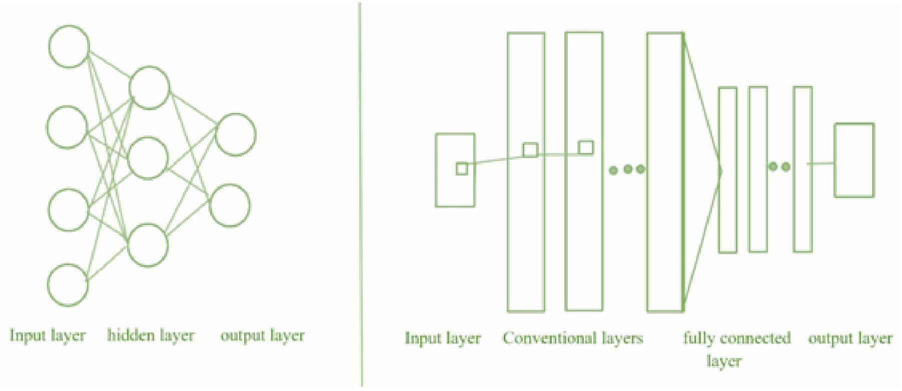

Figure 3.1: Basic components of the CNN in contrast with MLP [86].

These groupings are developed as compact layers. The central core of the neural networks is to maximize the weights of the kernel filter. In general, each hidden layer detects increasingly complex patterns for these convolution networks, starting with simplistic features and moving on to abstract complex pattern combinations, as the network goes deeper and closest to precisely determining output [54]. In its heart, CNN can apply both the classification and regression principle to the same problem. The CNN framework is generally used to classify images, localise objects or detect objects used on images from various sources. For this purpose, researchers use different architectures or networks to construct a useful generic model in the pipeline [62].

3.1.1 Basic Architecture

CNN's (convNet) simple concept consists of alternately layered blocks of convolutions and pooling layers and a final fully connected layer. The alternating convolution blocks are an output of the convolved filter(s) consisting typically of convolution layers and accompanied by batch normalization layers. New feature characteristics are learnt and stored by the individual kernel filter layer output at each composite block. The learning recognition becomes more complex until it reaches the top layer or block and class prediction nodes, as shown in Fig. 3.2.

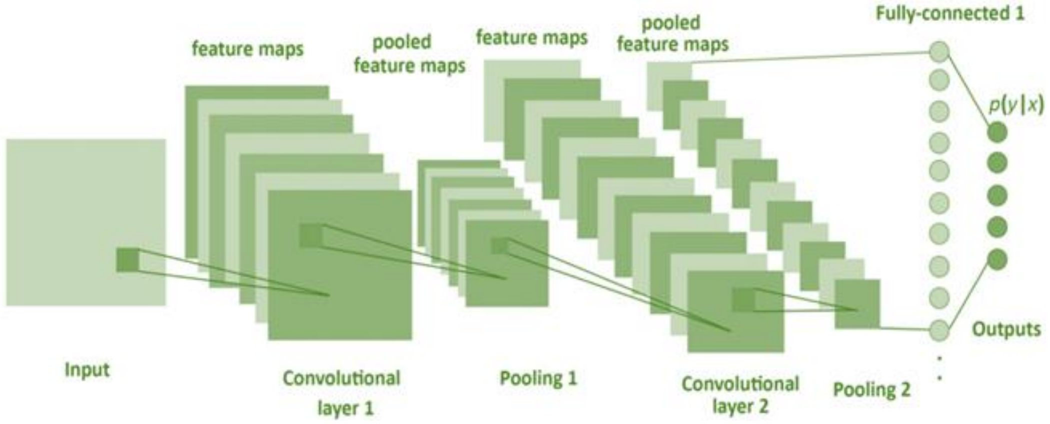

Figure 3.2: CNN with two convolutional layers, two pooling layers, and a fully connected layer, which allows for the final classification using class probability scores [50].

Convolutional layer

Convolution is a mathematical term that combines two functions to produce a third function as a matrix interaction [61]. The convolution layer is the central core of the ConvNet composed of filters (also kernel), applied across the image to learn and determine various features the network has acquired. The convolution layer computes the dot product's output between their weight and similar size positions in the input region from the previous convolution block [15]. Convolutions are executed by sliding the filter or weight over the input image to form the feature map. The feature map is the product bound to local patches representing the convolved filter's sliding over the previous layers [62]. The output of each convolution layer can be computed using the formular below:

$$c_m = f(W_m i_m + b_m) \tag{3.1}$$

where c_m is the output feature map (activation map) derived by the dot product between the input (preceding) convolution layer and all the filter with weight matrix W_m of kernel size $W \times H$, and b_m is the convolution layer's bias, and f represents the non-linear activation function.

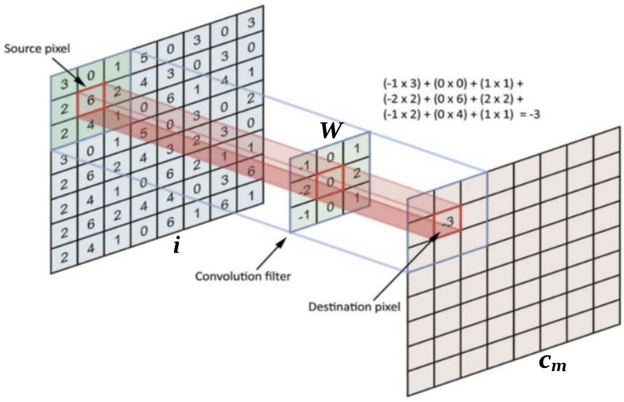

Figure 3.3: Interaction of Convolution layer [15].

The convolution process samples the image output by a feed-forward product based on the input image's filter size. To prevent this, padding, P is applied primarily to uphold the original input image size. It is just a mechanism by which the zero layers are applied to the image boundary. When the output function map is the same dimensions as the input image, it is referred to as the same padding, where no such padding is applied at all; it is referred to as valid padding. Also influencing the feature map size is the stride and depth. The stride, S refers to the step size taken when the kernel of size k x k slides over the input image while the depth describes the number of kernel filter which learns different image features and context. To ensure the image cover the full input image symmetrically, the following equation does the check [63]:

$$\frac{(I-k+2P)}{S} \tag{3.2}$$

Fully Connected Layer

This is where the final decision is made. The FC layer is usually situated at the end of a typical developed CNN's network architecture chronologically following several convolutions and pooling layers. The FC layer captures and positions the previous layers' output into n (class number) vectors inserted as the final step. Each number in this n-dimensional vector is likely to belong to one of the predefined groups (number of classes defined) [64]. If several FC layers are present, the initial layers are used to predict the right labels from the dot product of the final ConvNet and applied weight. The last FC layer then provides the final class probabilities for each label [65]. The last fully-connected layer uses the activation function to classify the input images' generated features into several classes based on the output sample. Neurons in an FC layer are connected to all the previous layers' activations, cognate to the multilayer perceptron (MLPs) output layer [63].

3.1.2 Gradient-Based Learning

Generally, most current training of convolution neural network (gradient-based learning) algorithms is based on three key elements: (i) forward computation, (ii) Loss computation, and (iii) backpropagation and parameter (weight) updating. The backbone of deep convNet learning utilizes a similar principle as the MLPs. The cost (loss) review functions and optimisation procedures determine the formation of useful convolution neural networks.

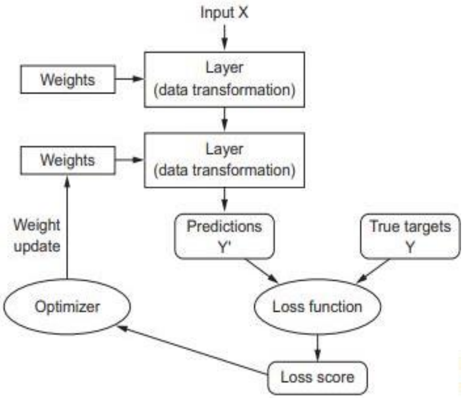

Figure 3.4: Gradient-based learning [62].

Forward Computation

In the forward computation, the input is supplied via the neural network architecture, which comprises interconnected layers (ConvNet), pooling, and fully connected layers as defined in the last subsection 3.1.1. Depending on the network architecture (classification or regression or both), the network generates the expected mark values (class probabilities or score).

Loss computation and Loss function

The network performance is improved by changing the parameter values, including weights and biases, acquired from the network. The optimization problem describes the complexity when deciding the optimum set of parameters that the loss function quantifies [66]. The loss function quantifies how much error the current weights produce. The nature of the loss function will be calculated according to the model's output units based on the cross-entropy between the data distribution and the model distribution [62]. For instance, the binary cross-entropy loss function is used for training models with sigmoid output units, whereas the categorical cross-entropy is used for training models with softmax output units [67].

Back Propagation

Backpropagation is a method to minimize the Error function (loss or cost). This function is based on the internal parameters of the model, i.e., weight and bias. The current error is typically propagated backward to a previous layer, where it is used to modify the weights and bias so that the error is minimized [62]. Weights are updated usually by the optimization function. The optimization functions measure the gradient (partial derivative) of the weight-loss equation and boost weights to the opposite direction of the measured gradient using the chain rule [68]. This loop is replicated until the global minimum is achieved.

A stochastically extracted input vector x abstracted in the form of a batch size of the training dataset is propagated over the network, layer by layer, to measure a $J(\theta)$ scalar cost once it reaches the output layer.

$$\mathrm{h} = f_1(\mathrm{x}, \theta_1) \qquad (3.3)$$

$$\hat{y} = f_2(\mathrm{h}, \theta_2) \tag{3.4}$$

$$\mathrm{J}(\theta) = \frac{1}{2}(\hat{y} - y)^2 \tag{3.5}$$

The vector x represents the input (image batch), which is then utilized by the hidden layer to output a vector, $\mathrm{h} = f_1\,(\mathrm{x}, \theta_1)$, where θ_1 is the kernel filter weight of the hidden layer. The output layer receives the hidden input vector, h, and generates the output value $\hat{y} = f_2\,(\mathrm{x}, \theta_2)$, and which θ_2 represents the weight of the output layer. f_1 and f_2 represent the activation function or classifier utilized to generate the output at the hidden and the final output layers. The scalar cost $J(\theta)$ is then backwardly distributed over the network, layer by layer until the first hidden layer is reached, to quantify the gradient of the network $\nabla_\theta J(\theta)$:

$$\frac{\partial J(\theta)}{\partial \hat{y}} = (\hat{y} - y)^2 \tag{3.6}$$

$$\frac{\partial J(\theta)}{\partial \theta_2} = \frac{\partial J(\theta)}{\partial \hat{y}} \frac{\partial \hat{y}}{\partial \theta_2} \tag{3.7}$$

$$\frac{\partial J(\theta)}{\partial \theta_1} = \frac{\partial J(\theta)}{\partial \hat{y}} \frac{\partial \hat{y}}{\partial h} \frac{\partial \mathrm{h}}{\partial \theta_1} \tag{3.8}$$

$$\nabla_\theta J(\theta) = \left[\!\left[\frac{\partial J(\theta)}{\partial \theta_1}, \frac{\partial J(\theta)}{\partial \theta_2} \right]\!\right] \tag{3.9}$$

The network's weights θ are updated based on the computed gradient as follows:

$$\theta_1 = \theta_1 - \eta \frac{\partial J(\theta)}{\partial \theta_1} \tag{3.10}$$

$$\theta_2 = \theta_2 - \eta \frac{\partial J(\theta)}{\partial \theta_2} \tag{3.11}$$

Some of the challenges of gradient-based learning include (i) Overfitting - where the model is good at understanding the training set but poorly interprets the test set, i.e., comparing the train loss/accuracy with the validation loss/accuracy. (ii) Vanishing and exploding gradients - The problem of the vanishing gradient describes the model learning is either very slow or ceases operating. In contrast, gradient exploding describes when the gradient signal increases exponentially, allowing learning to be unstable [69]. (iii) Hyperparameter tuning and model interpretability. Several optimization algorithms exist to make the training process faster, like Stochastic Gradient Descending (SGD) with momentum), Adaptive Gradient (AdaGrad), Root Mean Square Propagation (RMSProp), and Adaptive Moment Estimation (Adam).

3.1.3 Generalization of a model

A learning algorithm's strength is associated with its ability to generalize, i.e., handle unknown data. In addition to the generalization theory, there are two circumstances for model training: under-fitting and over-fitting [62]. Underfitting happens where the model trained is too straightforward to learn the data's underlying structure and fails to capture significant variables representing the reality of the situation being modelled [15]. In contrast, overfitting typically occurs in the case of complex models. Here the model learns unimportant information and makes noise more meaningful [64]. This may also be attributed to too many distinct classes (labels) at the output layer. Both conditions tend to make generalizations crappy. In under-fitting, a variety of approaches can be applied to fix it, such as using a more effective model with more parameters, having better functionality for learning algorithms, or reducing model limitations by reducing the hyperparameter for regularization [69]. In the case of over-fitting, certain approaches can be applied, such as simplifying the algorithm, minimizing the number of parameters (the use of additional parameters tends to contribute to a model that is vulnerable to over-fitting), gathering more training data (e.g., using data optimization techniques), and others. One or more loss functions are used to calculate this, which may vary based on the type of problem being faced. During the planning phase, the main goal is to reduce this shortfall.

Regularization

During training, models can sometimes find features or interpret noise to be important in a dataset due to their ability to memorize features concurrently. Consequently, there is a need to reach convergence, i.e., a level where the model optimally detects new tests or unseen data. Hence, regularization provides such a solution [15]. The aim is to minimize the amount of unpenalized costs considered a penalty term, consisting of other bias, and prefer a simplified model to minimize the variance and penalize larger weights. The penalized model involves trade-offs as it decreases uncertainty and therefore avoids overfitting. Several methods are suggested to regularize the model to avoid overfitting during training, utilized in this research. They include L1 and L2 regularization, drop out, the max norm regularizer, and data augmentation.

3.2 Image Classification

One of CNN’s most popular applications is possibly an image classification that attempts to identify the prevalent object type in an image dataset. Deep convNet utilized for image classification is based on the performance of convolution layers as its studies edges, patterns, context, and shapes resulting in a convolution feature map having spatial dimensions smaller and deeper than the original [64]. The progenitor of the image classification architecture referred to as feature extractor in object detection solutions is AlexNet with an 8-layer CNN, i.e., 5 convolutional layers + 3 fully connected layers developed by Krizhevsky et al. [70] in Imagenet challenge of 2012.

MobileNet

Mobile networks are lightweight deep neural networks. MobileNets and its derivatives were implemented to substitute a much deeper network constrained by the speed in achieving satisfactory output and real-time applications. This design’s idea is that the regular neural network convolution layer is broken down into two filters, depth-wise convolution and pointwise convolution [71]. The convolutional filter is more computationally complicated than depth-wise and pointwise convolutions. To achieve this model implementation, each channel is convolved with its kernel, called a depthwise convolution. Next, the pointwise (1 × 1) convolution is done to abstract and integrate the individual intermediate output from the depth-wise convolution into a single feature layer. Figure 3.5 shows the typical convolution form and the MobileNet way of convolutions. It is shown that depthwise separable convolutions, at lower computational cost, are a better solution to the problem.

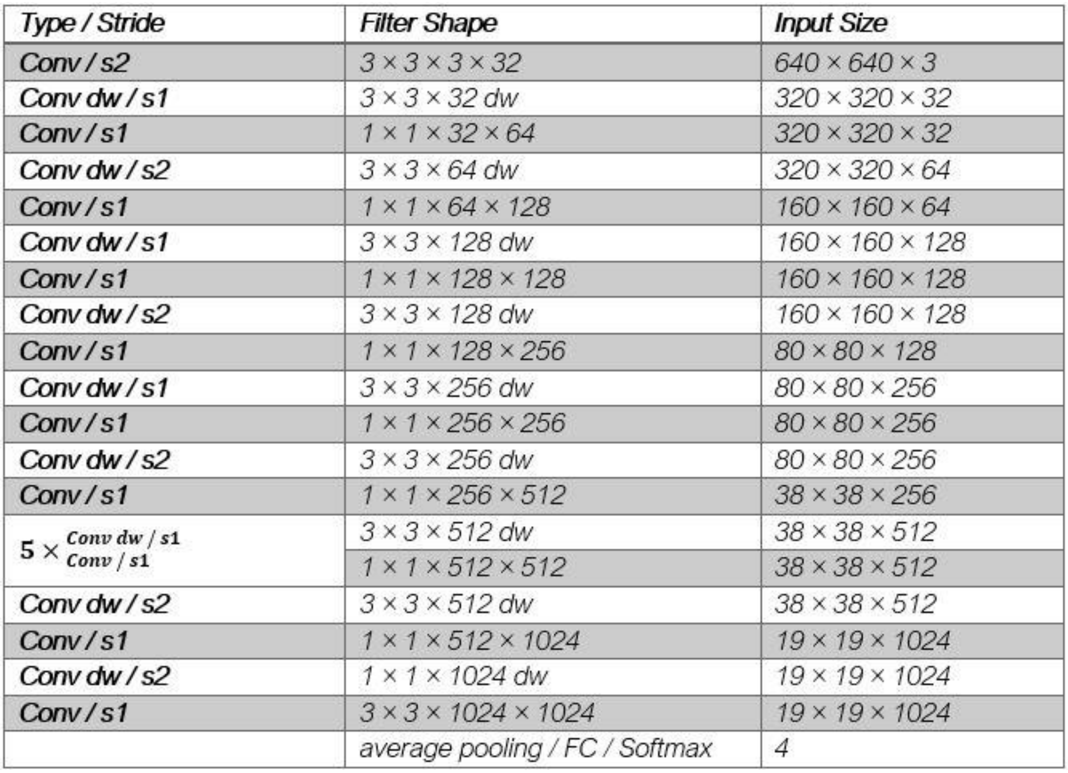

Type / Stride	*Filter Shape*	*Input Size*
Conv / s2	*3 × 3 × 3 × 32*	*640 × 640 × 3*
Conv dw / s1	*3 × 3 × 32 dw*	*320 × 320 × 32*
Conv / s1	*1 × 1 × 32 × 64*	*320 × 320 × 32*
Conv dw / s2	*3 × 3 × 64 dw*	*320 × 320 × 64*
Conv / s1	*1 × 1 × 64 × 128*	*160 × 160 × 64*
Conv dw / s1	*3 × 3 × 128 dw*	*160 × 160 × 128*
Conv / s1	*1 × 1 × 128 × 128*	*160 × 160 × 128*
Conv dw / s2	*3 × 3 × 128 dw*	*160 × 160 × 128*
Conv / s1	*1 × 1 × 128 × 256*	*80 × 80 × 128*
Conv dw / s1	*3 × 3 × 256 dw*	*80 × 80 × 256*
Conv / s1	*1 × 1 × 256 × 256*	*80 × 80 × 256*
Conv dw / s2	*3 × 3 × 256 dw*	*80 × 80 × 256*
Conv / s1	*1 × 1 × 256 × 512*	*38 × 38 × 256*
$5 \times \begin{smallmatrix} Conv\ dw\ /\ s1 \\ Conv\ /\ s1 \end{smallmatrix}$	*3 × 3 × 512 dw*	*38 × 38 × 512*
	1 × 1 × 512 × 512	*38 × 38 × 512*
Conv dw / s2	*3 × 3 × 512 dw*	*38 × 38 × 512*
Conv / s1	*1 × 1 × 512 × 1024*	*19 × 19 × 1024*
Conv dw / s2	*1 × 1 × 1024 dw*	*19 × 19 × 1024*
Conv / s1	*3 × 3 × 1024 × 1024*	*19 × 19 × 1024*
	average pooling / FC / Softmax	*4*

Table 3.1 Detail layer for MobileNet Architecture [71]

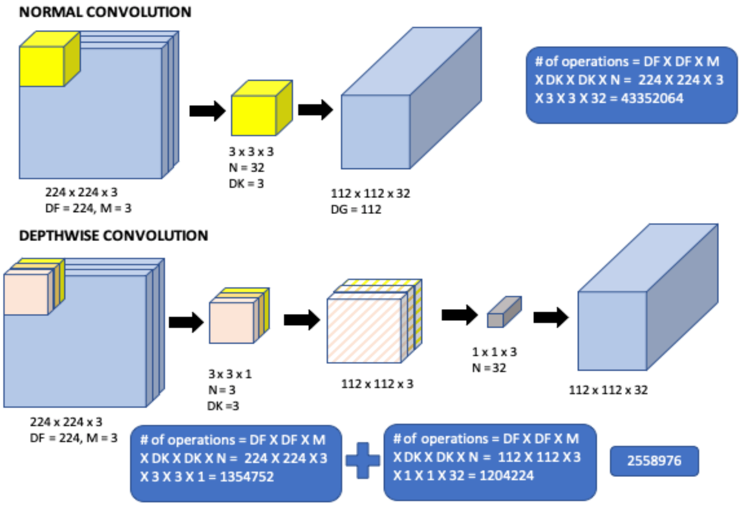

Figure 3.5: Concept of MobileNet results in lightweight CNN with 4.2 million parameters compared with VGG16 (138 million parameters) [71].

Resnet

Residual Network is also known as ResNet, which uses the concept of residual learning (by the subject of skipping). Residual networks were built with shortcuts to whole networks inspired by VGG networks [72]. To dissociate with the concept of increasing depth when creating CNN architecture, ResNet proposed a shallower network using shortcut connections, i.e., directly connecting the l^{th} layer's input to an $(l+x)$ layer. The significant ability to train very deep CNNs in 50, 101, and 152 layers with great successful connections are attributed to the regular cut-off's connection among the DCNN blocks. Necessary information of ResNets 50 and 101 are listed in Table 3.1.

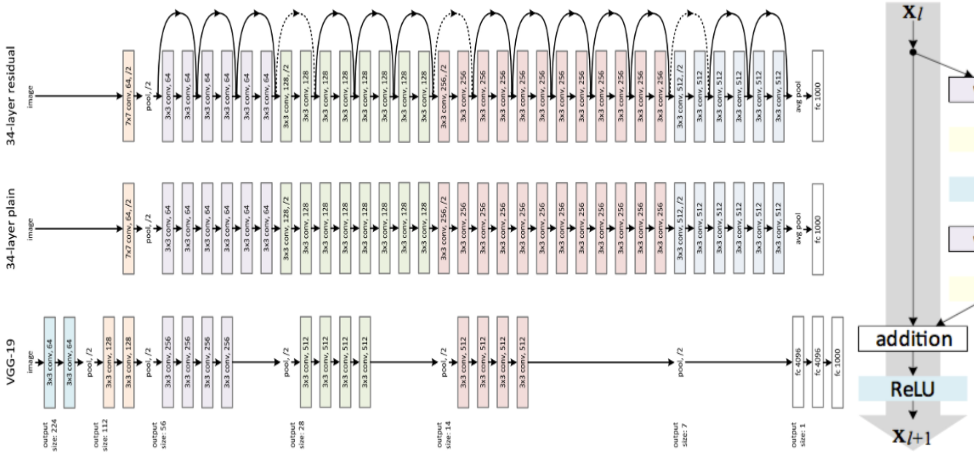

Figure 3.6: Architecture of ResNet [72] with the concept of a residual block (shortcut connections) [73]

Layer name	*Resnet50 (50-layer)*	*Resnet101(101-layer)*	*Output Size*
conv1	*7x7, 64, stride 2*		*112×112*
conv2_x	*3x3 max pool, stride 2*		*56×56*
conv2_x	$\begin{bmatrix} 1 \times 1, 64 \\ 3 \times 3, 64 \\ 1 \times 1, 256 \end{bmatrix} \times 3$	$\begin{bmatrix} 1 \times 1, 64 \\ 3 \times 3, 64 \\ 1 \times 1, 256 \end{bmatrix} \times 3$	*56×56*
conv3_x	$\begin{bmatrix} 1 \times 1, 128 \\ 3 \times 3, 128 \\ 1 \times 1, 512 \end{bmatrix} \times 4$	$\begin{bmatrix} 1 \times 1, 128 \\ 3 \times 3, 128 \\ 1 \times 1, 512 \end{bmatrix} \times 4$	*28×28*
conv4_x	$\begin{bmatrix} 1 \times 1, 256 \\ 3 \times 3, 256 \\ 1 \times 1, 1024 \end{bmatrix} \times 6$	$\begin{bmatrix} 1 \times 1, 256 \\ 3 \times 3, 256 \\ 1 \times 1, 1024 \end{bmatrix} \times 23$	*14×14*
Conv5_x	$\begin{bmatrix} 1 \times 1, 512 \\ 3 \times 3, 512 \\ 1 \times 1, 2048 \end{bmatrix} \times 3$	$\begin{bmatrix} 1 \times 1, 512 \\ 3 \times 3, 512 \\ 1 \times 1, 2048 \end{bmatrix} \times 3$	*7×7*
	average pool, FC, softmax		*1*

Table 3.2: Detail architecture of Resnet 50 and Resnet 101 [72].

3.3 Object Detection

Object detection follows the deep learning concept based on incorporating additional layers to neural networks to solve complex problems. Object recognition goes deeper and incorporates the idea of the image positioning of the object. It is a mixture of two tasks: object localization where bounding boxes are defined, which are made up of four variables (x-y-coordinate, width, and height) describing the rectangle that defines the object extent and the classification of the object within the selected bounding boxes to be uniquely defined [24].

The object detection follows the concept of the basic architecture of the CNN as discussed in section 3.1.1 and described by Equation 3.1 with multiple sliding windows capable of providing solutions to both the classification and regression problem. Multiclass object detection is enforced by thresholding the output feature maps, defined by several hyperparameters, to achieve the stated hypothesis to form a concrete response, i.e., an object class and a bounding box. However, this simultaneous localisation and classification process results in several instances labelled as objects, resulting in duplicate detections. Hence, the application of the non-maximum suppression (NMS) module to eliminate duplicate detection. In a nutshell, the resulting bounding box score with high-class score prediction was picked using a greedy strategy, and consequently, the remaining boxes with less than 50% overlap are deleted.

Various architecture has been developed for object detection, however choosing the best fit for any dataset is usually a herculean task because of the numerous base features used in extractors, different image resolutions, and various processing and computation trade-offs [74]. However, most custom-developed models are differentiated and chosen in terms of the trade-off between speed and accuracy. Several deep learning models implement object detection; however, based on these trade-offs discussed, the SSD [57] model is utilized in this study.

Single Shot Multibox Detector (SSD)

The SSD approach is focused on a feed-forward-based convolution network generating a fixed-size bounding box set and scores of object instances present in these boxes and a final detection process based on a non-maximum suppression criterion [57]. The early network layers are constructed on a standard image-classification architecture known as the base network (i.e., the classification layer without the flattened fully connected layer). SSD supersedes its counterpart, YOLO, by introducing several modifications: (i) multi-feature maps from subsequent networking stage are predicted to allow multiscale detection; (ii) object classes and offsets at bounding box locations are predicted using regular sized small convolutional filter; and (iii) after deriving final feature map, different predictors (classifiers) are used to identify objects at varying aspect ratios in the form of feature pyramids [75]. SSD's comprises two main parts: A feature map extractor (VGG 16 was used in the published paper, but ResNet or DenseNet can also be utilized to provide better results) and the convolution filter for object detection.

SSD attaches additional convolutional layers (feature layers), i.e., multiscale features and default boxes, which causes a steady decrease in size up to the end of the primary network. Hence, the predictions of detected objects are produced at multiple levels. Unlike YOLO, which uses a fully connected layer to make predictions, the SSD adds a series of small convolutional filters to each added feature layer (or an existing one in the base network optionally) and uses them in boundary box positions to predict classes and offsets of objects. SSD adds default boxes to various feature maps of various resolutions [57].

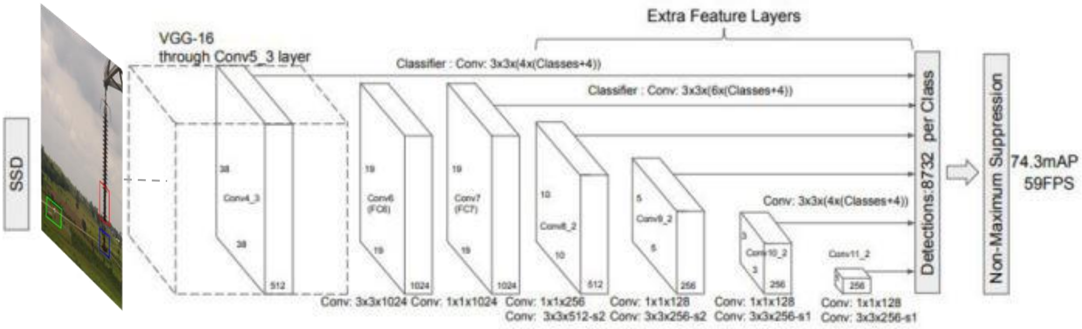

Figure 3.7: Architecture of SSD showing how the model adds several feature layers to the end of a base network, forecasting offsets to default boxes of varying sizes and aspect ratios and their corresponding confidences [57] [76]

4 Study Area and Datasets Used

4.1 Study Area

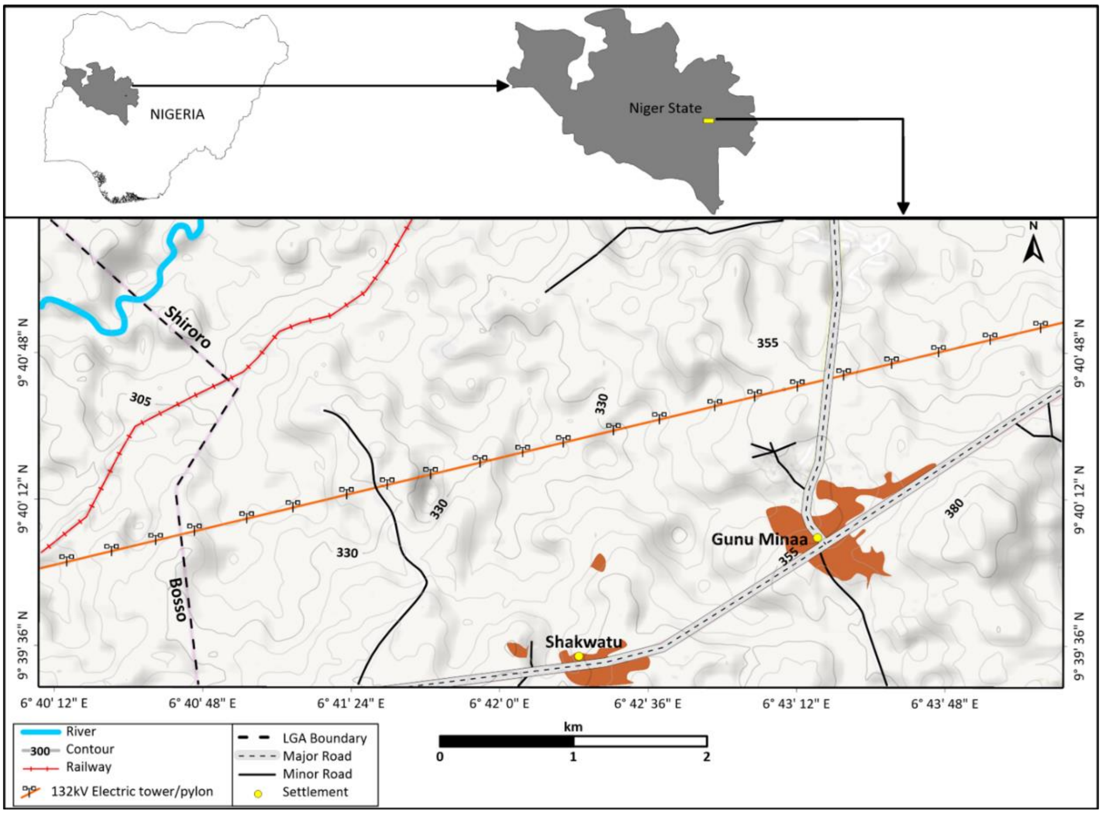

Figure 4.1: Study area with electric transmission line corridor

The study is based on the Shiroro - Kaduna Transmission Line corridor. The Shiroro-Kaduna corridor connects about seven states in northwest Nigeria. Nigeria lies between latitudes 4° and 14°N, and longitudes 2° and 15°E. The Nigerian Transmission Network, called the transmission company of Nigeria (TCN), deals with the transport of voltage in two phases, the 330kV - 132 kV and the 132kV-33kV along transmission lines (otherwise referred to as conductors). In general, all transmission corridor shares similar structure, their infrastructure is radial and thus causes inherent problems without redundancies. Even though several sources of power are abundantly available, on average, around 7.4%, network-wide propagation losses are high relative to the 2 - 6% benchmarks proposed for the developing countries and are majorly associated with asset maintenance [78], [79]. All of these represent vital infrastructure and market issues in the industry's subsector of transmission. In 2018, the industry struggled to distribute about 12.5% (5,000 megawatts) out of the amount estimated to support the population's basic needs [80]. This shortfall is also compounded by unannounced load shedding, partial and complete grid breakdown, and power failure mostly linked to the transmission company. Consequently, Nigeria's energy sector generates, transmits, and distributes megawatts of electric power substantially less than what is required to satisfy basic household and industrial needs, indicating the need for substantial investment to improve distribution efficiency.

4.2 Datasets used

The DJI Phantom (DJI FC330) fitted with high-resolution cameras was flown across the Shiroro-Kaduna T.C.N. network of 111-132 kV overhead transmission lines (7km) for the capture of pylons, conductors, elements of power line/pylon accessories (e.g., insulators, fittings, cross arms) and the objects surrounding (e.g., vegetation) from a range of angles of images. The sensor provided three spectral bands with a high spatial resolution comprising of the visible RGB. The products had been acquired by an aerial survey conducted from October 12, 2020, to October 22, 2020. In the event of lost or compromised images of transmission towers, the images were discarded. A total of 140 images covered the study area and can be characterised as high-resolution oblique RGB images of dimension 4000 x 3000 pixels (72dpi). The mean pixel sensor resolution is 0.00124m. Generally, within the images' most prominent objects are located and systematically distributed transmission conductor and pylons with dirt roads, small patches of natural forest, and grasslands.

4.3 Taxonomy of faults

Inspection of power line components is a primary activity for utilities and one of the most common research needs in power line inspection. The purpose of this task is to detect and classify the faults found in the transmission components. Many components are connected like pylons, conductors, and pylon accessories or fittings (e.g., insulators, dampers, and fixtures), and each type of component has different faults.

Pylons are pillars used for the extension of conductors over large areas, support lightning safety cables and other transmission elements, ensure proper electrical transmission process of the other components by preserving the original design positioning, and provide sufficient grounding against adjoining objects. Insulators are critical elements in a transmission system as they protect conductors by allowing lines to retain their expected electrical insulation strength [18]. As seen in Figure 4.3, the insulator has a repetitive, stacked cap structure. The colour, size, and string numbers of the insulators vary based on the transmission capacity and manufacturing design (e.g., single string and double strings). The pylon accessories, also called fittings, are the connectors of major components or elements seen in the electricity transmission lines. They mainly serve as support, inhibitors, connectors to the other transmission components. These include conductor clamps, dampers, splicing fitting, protective fittings, and guy wire fittings.

Consequently, most of these individual components have many different types of faults. For this research, the defects were divided taxonomically into four categories: missing insulator, broken insulator, rusty clamp, and broken dampers according to the contents of the captured aerial photographs. The detailed fault taxonomy discussed in this study is as follow:

i) Missing Insulator: These are those glass insulators with missing insulator cap (plate); see Figure 4.2.

Figure 4.2: Missing glass insulator faults

ii) Broken insulator: This applies to those insulators made of porcelain or composite polymer plate or cap materials. In this fault, the plate is incompletely destroyed by pressure exerted by external forces such as weather, especially thunder-strike and thaw.

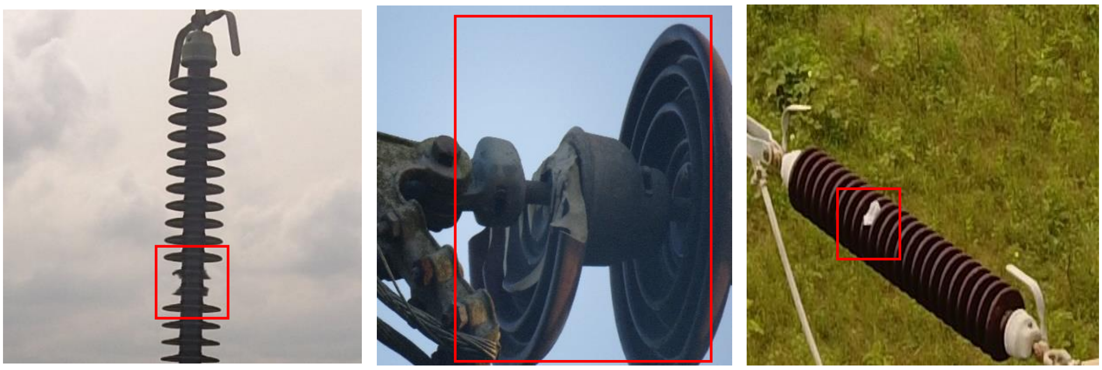

Figure 4.3: Broken insulator faults prominent with the porcelain or composite plate type insulator

iii) Rusty clamp: The conductor clamp, i.e., strain or suspension clamp, helps to hold all components, especially the insulator, to the tower architecture based on its design. A faulty clamp can lead to the insulator's total malfunction, hence leading to transmission collapse.

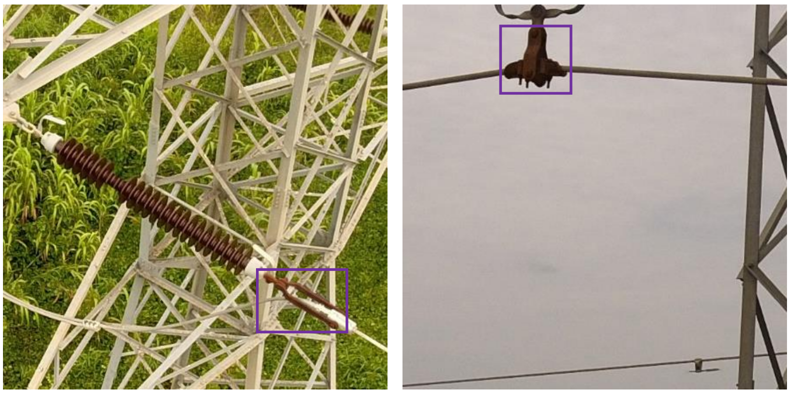

(a) *(b)*

Figure 4.4: Rusty strain (a) and suspension (b) **clamp**

iv) **Broken Fitting**: Here, the fitting considered was the vibration damper without which causes conductor fatigue and strand breakage.

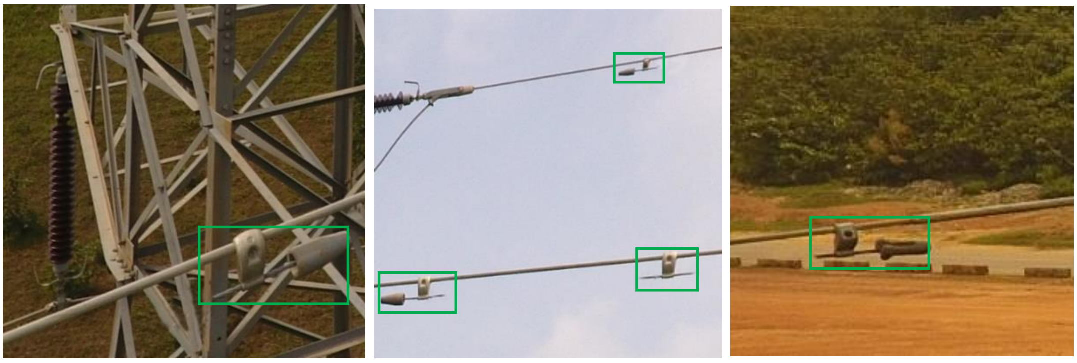

Figure 4.5: Broken fitting (vibration dampers)

5 Methodological Description

In this project, a solution was developed for the automatic vision-based detection of electric power line component faults using UAV optical images and deep learning architecture. The deep learning approach was adopted because of its ability to characterise intricate patterns in remote sensing imagery such that images with many variations in context and viewpoint are efficiently learned, and small-scale objects are identified from the limited datasets. The outline of the method can be seen in Figure 5.1. For this electrical fault classification and detection, SSD, a one-stage detection model, is considered with varying base ConvNet network architecture, i.e., the backbone for feature extraction. A naïve strategy for object detection is to use a sliding crop-based window moving across the image. A preferred modification of this method is using a Region-based proposal adopted by the Faster RCNN model. However, there are drawbacks to this method: i) they are computationally expensive as each 2000 proposal from selective search goes through its block of the convolutional neural network [55], and (ii) requires three models to train any dataset.

Hence, the SSD was chosen based on its ability to balance processing time, speed, and accuracy. Three different pre-trained models are utilized for the base network to develop the model: ResNet-50, ResNet-101, and MobileNet. The first network architecture utilized will be referred to as SSD Rest50. The second CNN architecture is indicated as SSD Rest101. Similarly, the third form of CNN base network is assigned the name SSD MobNet. The three variations of the base network CNN have been employed to analyse how the detection accuracy varies with the change in base network architecture.

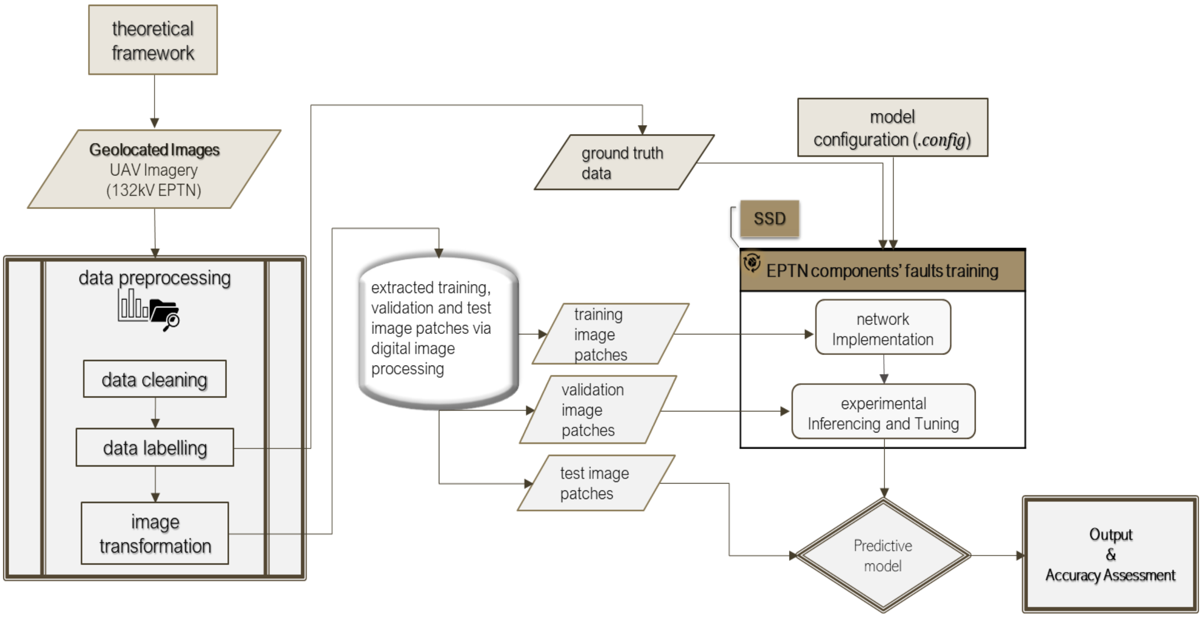

Figure 5.1: Methodology Workflow.

5.1 Data Pre-processing and labelling

The whole dataset contains 294 images. Due to the small-scale problem identified in some research [58], the dataset (132kV) was split into about 817 tiles centred on at least one components' fault of interest. For the other dataset representing the other 33kV transmission line, the non-destructive resize, i.e., resize and pad approach, is applied to preserve the image aspect ratio to preserve the geometric and spatial information. Moreover, the split and resized RGB images were normalized to the same size of 600 x 600 pixels following [33], combined to form a total of 1027 'Felect' dataset sample imagery. The data is divided into train, test, and validation sets. It was assured that 17% of the original dataset was allocated for the test dataset, and 83% of the dataset was reserved for training and validation. About 80% of training was used as the training samples, while the remaining 20% was dedicated to validation samples - table 5.1 displays the data slicing information. The drone captured the 'Felect' dataset with numerous characteristics, including diverse perspectives, sizes, occlusion, background clutter, and intra-class variance.

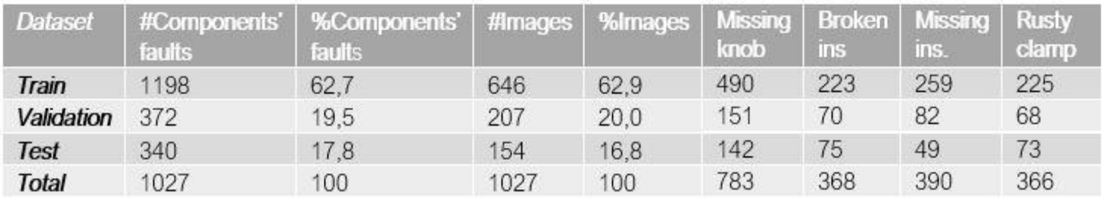

Dataset	#Components' faults	%Components' faults	#Images	%Images	Missing knob	Broken ins	Missing ins.	Rusty clamp
Train	1198	62,7	646	62,9	490	223	259	225
Validation	372	19,5	207	20,0	151	70	82	68
Test	340	17,8	154	16,8	142	75	49	73
Total	1027	100	1027	100	783	368	390	366

Table 5.1: Data partition

Thus, a "stratified" data division is used, making the proportion of the faulty components' for the dataset similar to the number of images, as well as the average number of components and the intraclass variation shared equally for samples with different types of difficulties to be learnt and appropriately located and classified.

Data annotation is utilized to identify and label the output sample layer used in supervised learning. An annotation is the means of digitising the set object of reference. The bounding box approach and pixel-wise object segmentation are two approaches that can be used to annotate the main object on the image manually. To annotate the faults as partitioned, the ground truth annotation of actual components' fault types was generated as a rectangular bounding box mask was then drawn around the object rendering the object within the box for each image in the datasets. LabelImg tool is employed to label the different component faults as displayed in section 4.3. The details of the image, bounding box, and object class, along with shared characteristics, were stored as a VOC2007/extensible mark-up language (.xml) file. After annotating all the frames, the whole split dataset containing image patches tensor and their output label were converted into a TF record-oriented binary as shown in Figure 5.2 to help dataset initialization and ease network architecture using the TFRecordWriter function.

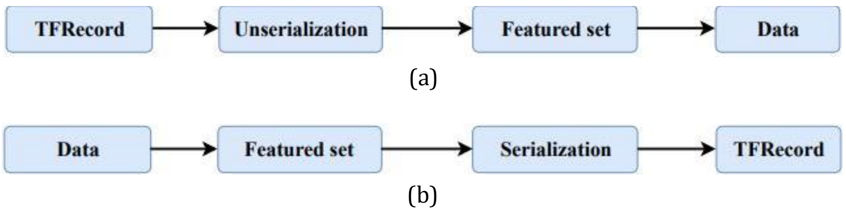

(a)

(b)

Figure 5.2: TFrecord (a) reading and (b) writing principle.

5.2 Network Training

As stated in section 5.1, input patch images are first translated to tensors (TF records) with a [600 x 600 x 3] form prior to feeding it into the backbone architecture and are distributed by the action of the convolution layer to an intermediate layer consisting of a convolutional activation map. The head of the network architecture (backbone network) is explained in sections 3.2 and 3.3 and typically follows the patch-based CNN architecture. Therefore, image patches that contain either a single class of faults or a combination of different components' faults centred in the pixel of interest, also termed as valid patches, were extracted. For, backbone neural network ResNet50, MobileNet, or ResNet101 are utilized for the first part of the SSD network as the head to develop three models.

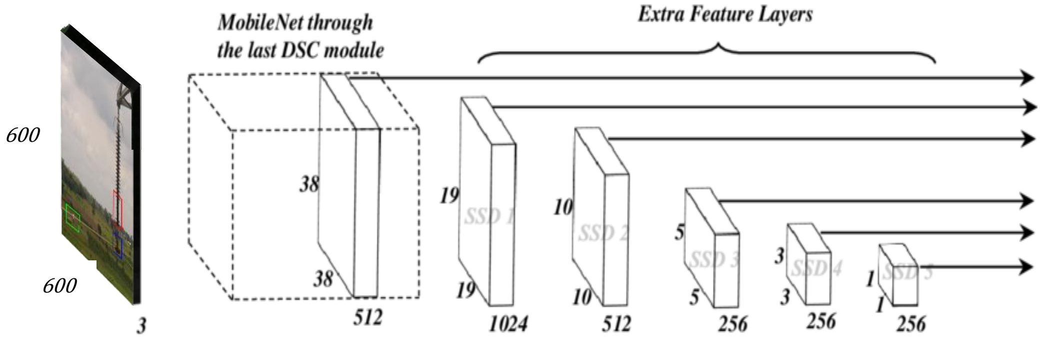

Figure 5.3: Model architecture [52].

This head is made of CNN that detects smaller characteristics (patterns and corners), and later layers detect higher characteristics successively. The image was resized first into 640px x 640px x 3 (RGB) and then translated into a *38 x 38 x 512* characteristic mapping through the backbone network passed to the Conv7 denoted as SSD 1 (auxiliary layer) in Figure 5.3. In all experimentation cases, the input patch tensor was abstracted into multi-level representations to classify the different faults after going through the backbone architecture (without a fully connected layer). As a deep neural network, the backbone algorithm derives semantic significance from the image while maintaining its spatial structure.

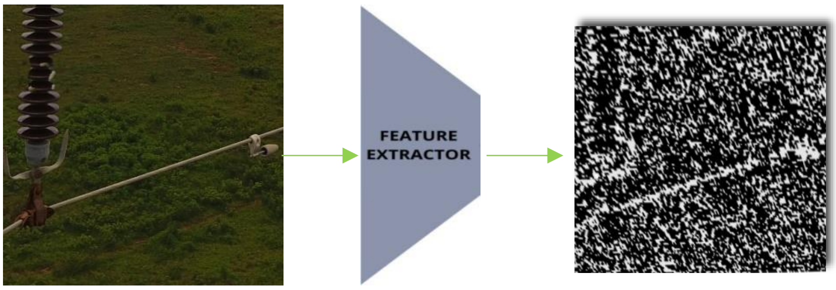

Figure 5.4: Input image patch and corresponding feature map generated by the feature extractor (backbone architecture).

The series of auxiliary convolutional layers (SSD layers) introduced after the SSD model's backbone allows the extraction of features at different scales as the input feature map decreases at each successive layer. This ensures the certainty of boundary variance and class prediction of targets at various scales. For each decreasing successive auxiliary layer (multi-scale feature maps), SSD networks grids the image and assign each grid with the task of detecting objects. After this, 3 × 3 convolution filters are applied to each cell to make predictions. If no object appears, the context class is not considered, and the location is ignored. Each cell in the grid will decide the location and shape of the object inside it.

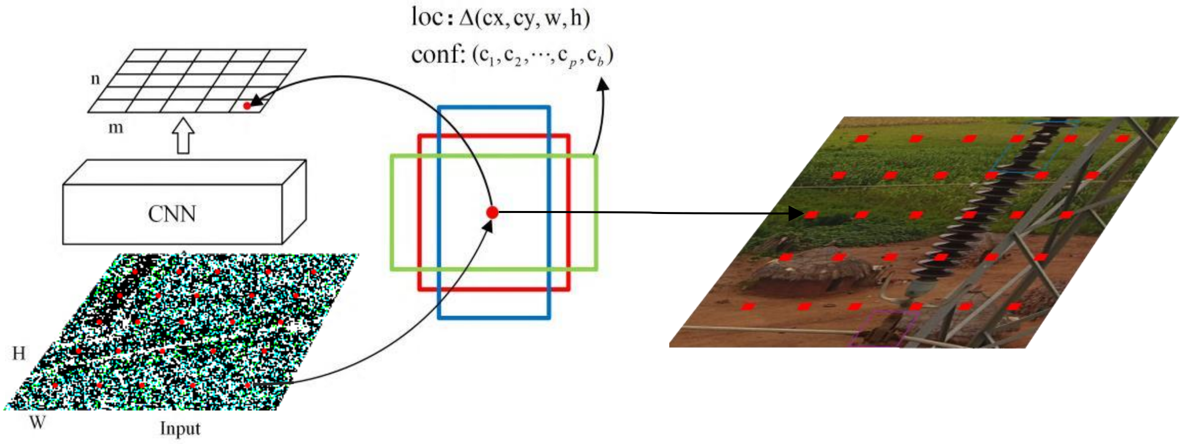

Figure 5.5: The default boxes generation for one cell over the backbone network feature map.

Immediately after gridding the auxiliary layer, i.e., feature map at multi-level, default boxes are generated at each grid cell for each convolution layer level using a defined scale value. This scale increases progressively towards the least spatial resolution feature map level (SSD 5). Next, bounding boxes are generated via a process called default box generation (prior). Default boundary boxes are selected explicitly, which are pre-computed, fixed-size boxes that closely fit the ground truth boxes. With the different experiment scale values, s_k, and the aspect ratio, $ar \in \{1.0, 2.0, 0.5\}$, the default box sizes are built. To detect larger objects, SSD uses lower resolution layers such as the SSD 4 and SSD 5 layers in Figure 5.3. Each grid prediction composition includes a boundary box defined by b_x, b_y, b_w, b_h, and four scores for each class, i.e., components faults, in the prediction, with the highest-class score associated with the positioned default bounding box. The class score corresponds to object classification labelled in this research as "broken insulator," "missing insulator," "missing knob," and "rusty clamp." Having these several forecasts at once and awarding class scores to each is referred to as the Multibox. There are four predictions for every cell, regardless of the feature map's spatial resolution, and an extra one prediction to represent objectness.

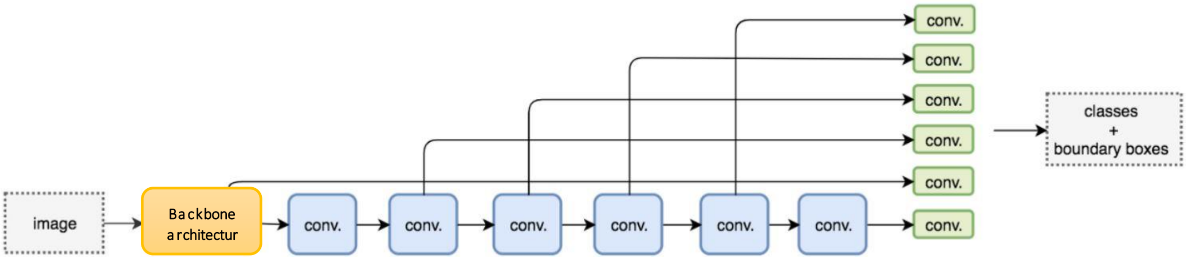

Figure 5.6: Multiscale downscaling layer (auxiliary layer) concept.

To improve the SSD to detect small-scale faults type, the Feature Pyramid Network (FPN) training structure is used in conjunction with the most immediate output feature map activated from the base network architecture. This method also imbues low-level CNN layers with more assertive semantic representation, such as layers near its head to detect small-scale object labels. In particular, the default boxes are chosen so that their Intersection over Union (IoU) is greater than 0.6.

The Sigmoid function is then performed on the output feature map generated by the last CNN to obtain a class prediction score. Thereafter, the total loss is achieved by combining the two losses obtained for backpropagation. The two new losses measured by the network for each bounding box include:

a) The localisation loss is achieved using the weighted smooth-L_1 loss, calculated by comparing the generated default boxes (prior) against GT labels.
b) The confidence loss is achieved using a similar method applied in image classification, in this case, the weighted sigmoid focal.

The default boxes that did not get scored against any ground truth boxes are viewed as negatively matchbox and are applied to only the confidence loss, while the positive box is applied to the overall loss. This loss value is backpropagated to update the network parameters using different optimizers during experimentation.

5.3 Experimental Settings

The current projects' fundamental problems were related to the number of computing resources required and the dataset's limited size. In this study, the experiments - backbone architecture and meta-architecture were built on the top of the deep learning framework of TensorFlow Object Detection API (TF 1) Model Zoo[1]. Two separate outlets were utilized for execution, they include:

i. A physical system with AMD Ryzen 5 3550H with Radeon Vega Mobile *Rfx* processor CPU with 7.81 GB for data processing, preparation, and model testing.

---

[1] The source code of this implementation can be found at: https://github.com/EmekaKing/Felect

ii. Google Colab on the Google cloud server with 2 Intel(R) Xeon(R) @ 2.20GHz processor CPU with 13GB RAM (200 GB free space disk) and 1 GPU (Tesla K80) with 12.6 GB RAM for parallel processing for experimentation.

To ensure optimal experimentation with the data available, the validation dataset covering the research assets was utilized for evaluating the trained network. Due to computation cost and speed, the k fold cross-validation was not implemented. Hence, a hold-out validation with shuffling was used to generate an average detection result for all the models.

The training set was used during network training, while the validation dataset was used to modify hyperparameters. In the NMS process, 100 detections and an IoU threshold of 0.6 were maintained for each class. The momentum and the batch size were set as .9 and 8. The regularization value was set to 0.0004. The warm-up learning rate of 0.0001333 was used to assist in the weight optimization after 5,000 training steps and at the end of the training period decay to zero. Batch normalization (BN) is used after the convolution layer and before nonlinearity layers [81] to avoid overfitting and to save time during hyperparameter tuning. During training, the data augmentation technique increases samples' diversity because of insufficient training data. Six methods were employed for this data augmentation in the training phase: jitter boxes, horizontal flip, vertical flip, crop, pixel value, and rotation. To ensure guaranteed detection, the IOU confidence level is set at 0.6. Five measurements, including recall, precision, f_1 score, and mAP, are applied to evaluate the components' faults model performance.

Hyperparameters	Values
Momentum	.9
L_2 regularization	0.0004
Batch size	8
IoU -Threshold	0.6
Min and max scale	3 - 7

Table 5.2: Training hyperparameters settings for CNN models

5.4 Sensitivity to Hyperparameters

In this study, the hyperparameters examined were learning rate optimizers and the aspect ratio (Table 5.3). During the experiments, when the value of one hyperparameter is modified, other hyperparameters are retained continuously to achieve the optimum value of the hyperparameter.

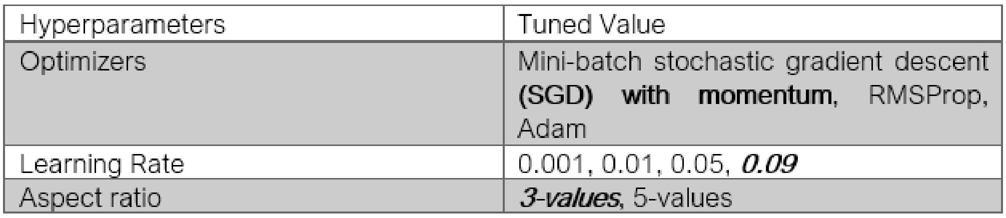

Hyperparameters	Tuned Value
Optimizers	Mini-batch stochastic gradient descent **(SGD) with momentum**, RMSProp, Adam
Learning Rate	0.001, 0.01, 0.05, ***0.09***
Aspect ratio	***3-values***, 5-values

Table 5.3: List of DCNN experiments on hyperparameters tuned using hold-out validation. The bold font shows the final chosen values from the hyperparameter settings.

Optimizer

In MLP and CNN architectures, optimizers determine the extent to which the loss function is minimized. An optimizer is a function that updates the model parameters to improve accuracy [82]. Updates to weight will vary with each preference of the optimize. Three optimizer algorithms were chosen to test the efficiency of the three proposed components' faults architecture: mini-batch SGD with momentum, RMSProp, and Adam.

Learning rate

Learning rate is a hyperparameter used to monitor how easily the model weight can be improved to learn optimally the problem modified. It is amongst the most critical tuning parameters to change when training a neural network. The research explored the impact of the learning rate by varying its values while keeping other parameters and hyperparameters constant.

5.5 Performance Evaluation

To achieve this, the SSD model is evaluated using several performance metrics against the validation data set regarding the ground truth. The models' experiments were measured using mAP metrics achieved over the validation dataset to select the optimum hyperparameters. Following these experiments, the models were chosen for final training and detection of the test data set using the best hyperparameter combinations. The detection results were also significantly measured by metrics such as the mAP and F_1-score statistics data. Generally, these metrics are based on four evaluation outputs: true positive (TP), false positive (FP), true negative (TN), and false negative (FN). For this research, components fault identification is considered a multiclass object detection. Details of these four fundamental evaluation quantities are described and expressed below:

- True positive (TP) = number of correct detections of component fault types with IoU > 0.5.
- False positive (FP) = number of correct detections of component fault types with IoU ≤ 0.5 or detected more than once.
- True negative (TN) = negative ground truth boxes having IoU ≤ 0.5 or no intersection with detection boxes of component fault types.
- False negatives (FN)= number of component fault types not detected or ignored ground truth boxes.

Precision and Recall

Precision refers to the ratio of the positive object correctly classified and localized to all positive classification. In other words, precision is a measure of how many positives are expected. The recall applies to all localized and classified observations that belong to the ground truth's insitu class [83]. Precision is affected significantly by FP, and FN's cost

(5.1)

determines the recall performance of any model. Precision and recall can be determined as:

$$Precision = \frac{TP}{TP + FP}$$

$$Recall = \frac{TP}{TP + FN} \tag{5.2}$$

F1-Score

F_1-score is the harmonic means of precision and recall. It considers both false positives and false negatives. These calculations are usually more straightforward where there is an unequal class distribution (many negatives). F_1-Score is computed as:

$$F_1 - Score = 2 \times \frac{Precision \times Recall}{\text{Precision} + \text{Recall}} \tag{5.3}$$

mAP

AP is the precision averaged across all recall values between 0 and 1. Averaging the AP, also termed mean average precision (mAP), serves as a significant metric to measure object detection models' efficiency and accuracy. mAP measures all classes' average precision over the model's recall rate, i.e., between 0 and 1 value representing the area under the Precision-Recall-Curve (PRC) [83]. The precision and recall of the observed boundary boxes and their values vary between 0 and 1, with a higher number indicating a good rating. The mAP is a reasonable indicator of network sensitivity and is based on the intersection over union (IoU) or Jaccard index [55]–[57]. The IoU is the ratio between the ground truth and the forecast area to the overall area or area of the union as shown in Figure 5.7 and is given as follows:

$$IoU = \frac{\text{Area of Overlap}}{\text{Area of Union}} \tag{5.4}$$

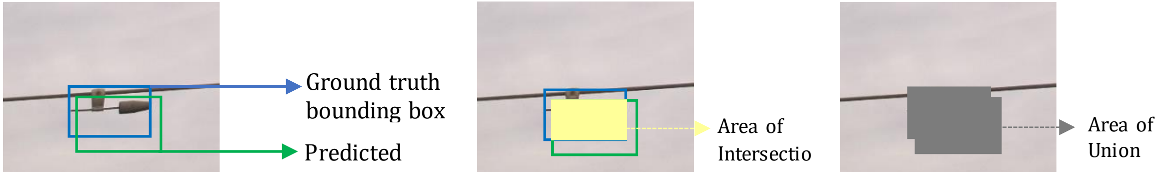

Figure 5.7: IoU concept (Jaccard Index).

In this way, detections are attributed to objects' ground truths and assumed to be true or false positive by overlapping the boundary frame. The overlap between the expected boundary box and the ground truth bounding box must reach 50% to be called a correct detection.

A five-stage procedure where the mean average precision of a class is calculated is as follows [84]:

a) Calculate precision (the proportion of true positives, i.e., component fault existing)

b) Calculate recall (the proportion of good positive out of all events)

c) Compute the Precision x Recall curve for the various thresholds. For this, we must first order the detections by their confidences, then determine the precision and recall for each cumulative detection.

d) Average the overall precision value for all recall stages. By Interpolating over all data points or an 11-point interpolation, i.e., by calculating the precision of the eleven recall stages evenly spaced [0, 0.1, 0.2, ..., 1.], the average precision score for each class is:

$$AP = \frac{1}{11} \sum_{Recall_i \in \{0, 0.1, \dots, 1.\}} Precision(Recall_i) \tag{5.5}$$

e) Finally, the mAP is determined by taking the average AP for all classes and/or IoU thresholds. The mAP is approximated AUC of the Precision x Recall curve. In the current project, only one IoU threshold (mAP@0.5) is considered.

6 Result and Discussion

In order to check the detection performance of the SSD model, it was first reviewed based on its performance to detect other particular features of the object. Therefore, before enhancing the whole network's efficiency, it was essential to run the proposed approach in isolation using the default settings. Second, the different backbone was implemented and contrasted with each other and compared based on the change in hyperparameters. Using some related checks, the efficiency of different models in detecting EPTN faults was measured. Three experiments were conducted, including the optimizer out-turn, learning rate sensitivity, and the effect of aspect ratio.

6.1 Analysis of Experimenting DCNN Hyperparameter

Influence of Optimizers

Although the original SSD[2] employed momentum as the optimizer, two other approaches were tested to evaluate the model's effectiveness. This study demonstrates that momentum is best to be used for further evaluation and model development.

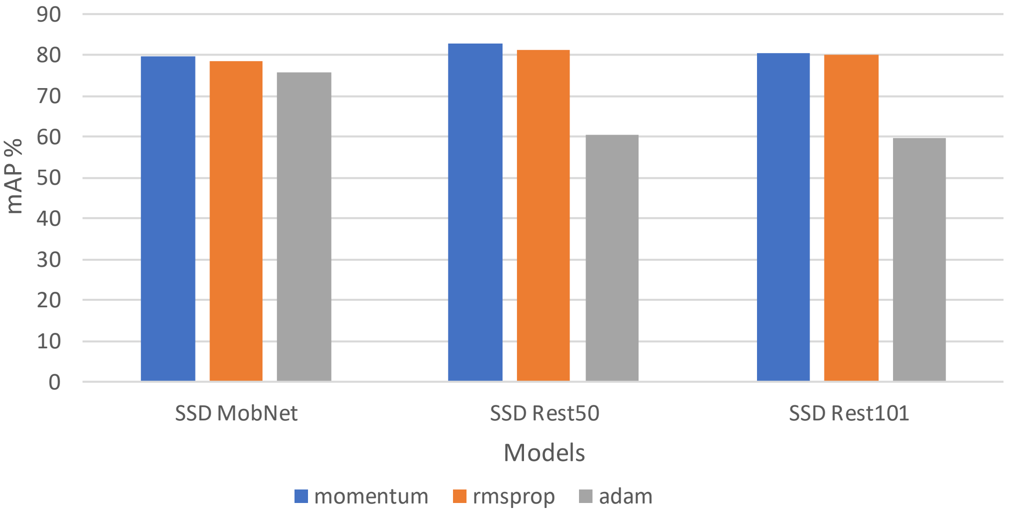

Figure 6.1: Effect of varying optimizers.

Figure 6.1 demonstrates how the different models performed during experimentation when different optimizers are applied. It was observed that the momentum optimizer gave the best mAP across the different models using the default hyperparameter settings (with learning rate = 0.05 and aspect ratio scale = 4.0). SSD Rest50, SSD Rest101, and SSD MobNet achieved a mAP of 82.85%, 80.42%, 79.61%, respectively, using the momentum optimizer. The SSD Rest50 gained the highest mAP when compared to the other two models. Also, it can be seen with the momentum optimizer, the validation and

---

[2] The source code of this implementation can be found at: https://github.com/EmekaKing/Felect

total loss converge optimally. Furthermore, it has been expressively proven that the model's convergence is affected by the optimizer utilized, as seen in Table 6.1.

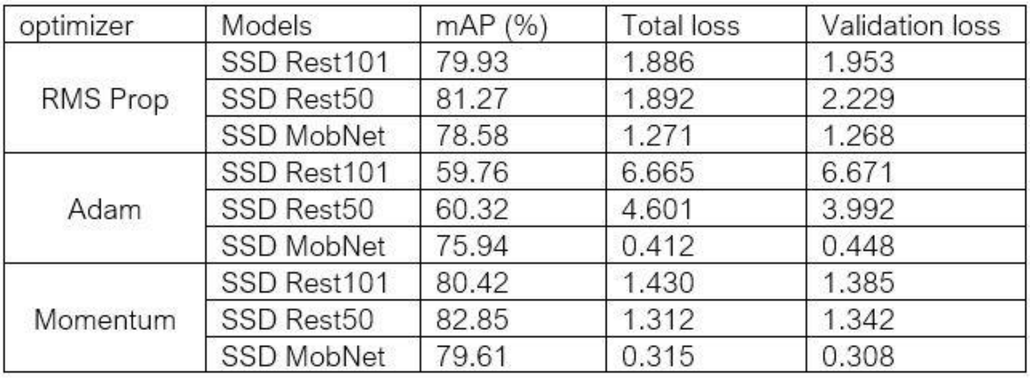

optimizer	Models	mAP (%)	Total loss	Validation loss
RMS Prop	SSD Rest101	79.93	1.886	1.953
	SSD Rest50	81.27	1.892	2.229
	SSD MobNet	78.58	1.271	1.268
Adam	SSD Rest101	59.76	6.665	6.671
	SSD Rest50	60.32	4.601	3.992
	SSD MobNet	75.94	0.412	0.448
Momentum	SSD Rest101	80.42	1.430	1.385
	SSD Rest50	82.85	1.312	1.342
	SSD MobNet	79.61	0.315	0.308

Table 6.1: Influence of using varying optimizers.

We can also observe based on Table 6.1 that all the optimizers attain acceptable rates of mAP, but one of the most glaring differences in the value of training loss and validation loss as well as the model convergence, i.e., the degree of loss range from zero. It can be inferred that the optimizer momentum with cosine learning rate is the one that provides the best results and the quickest to converge.

Learning rate effect

Using Momentum as the ideal learning algorithm, numerous learning rate settings were checked to improve the model performance. After several preliminary evaluations, it was confirmed that the best initial Learning rate (Lr) was 0.09.

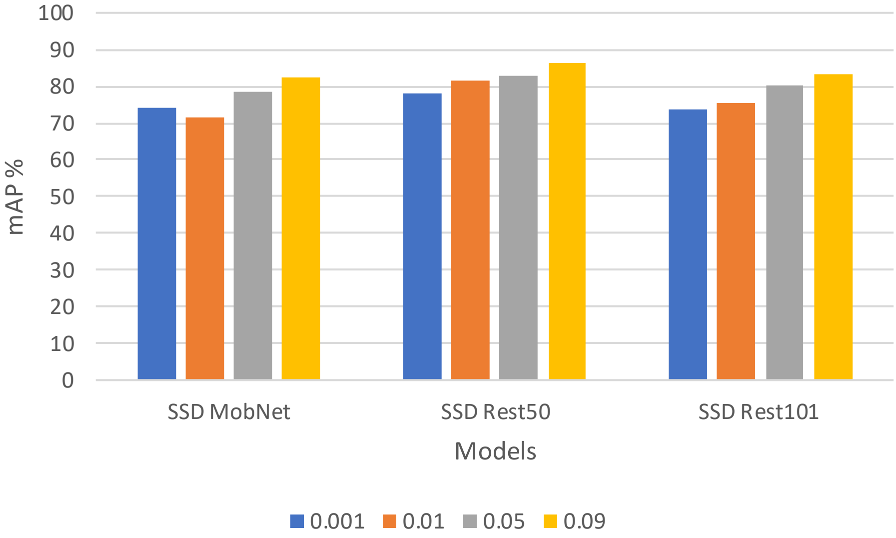

Figure 6.2: The accuracy achieved using varying learning rates.

The learning rate detection results are presented in Figure 6.2, with the aspect ratio scale is set to 4. The first model, SSD MobNet, reached a mAP of 73.94%, 71.56%, 79.61%, and 82.52%, with the learning rate was 0.001, 0.01, 0.05, and 0.09 respectively, better performance of the model with increasing learning rate value. Similarly, the remaining two models: SSD Rest50 and SSD Rest101, demonstrated the greatest average mAP of 86.29% and 83.14%, with a learning rate of 0.09, which is 3.44% and 2.72% higher than those obtained when set to 0.05. The learning rate plays a significant role in the network's performance and how easily it can generalize [82]. Specifically, decreasing the learning rate beneath this value (0.09), which gives the fastest convergence outcomes, will improve the mAP to generalize, particularly for large, dynamic cases. The learning rate used for all models was 0.09 as they all performed quite well with this value.

Effect of as aspect ratio

The grid default generated by SSD is based on stride, scale, and aspect ratio, making these factors one of the essential hyperparameters. The validation data was used to demonstrate the model's conduct due to variations in the aspect ratio hyperparameter. As a reminder, the number of scales multiplied by aspect ratios equals the total number of anchors (priors) for all possible variations of the four components' fault classes.

Aspect ratio	**mAP (%)**		
	SSD MobNet	SSD Rest50	SSD Rest101
[0.5,1.0,2.0] (default)	82.5	86.2	82.6
[0.5,1.0,1.5,2.0, 2.5]	38.7	44.3	37.2

Table 6.2: Effect of anchor aspect ratio.

Based on the findings from data exploration of the images, it was possible to infer that the fault ground truth's aspect ratio ranged from 0.5 to 3 after splitting into 600 by 600-pixel tiles. However, the patch size is rescaled for the model, affecting the rendered image's final aspect ratio. The findings shown in Table 6.2 show that adding an extra aspect ratio value does not achieve a greater mAP than the base aspect ratio. With the inclusion of a fourth and fifth dimension, the mAP decreases. Also, it can be seen that using only three aspect ratios is sufficient to detect components' fault classes in the images denoting the bounding boxes are appropriately readjusted to the ground truth boxes using the losses from localization and categories output of the object detector.

6.2 Performances of the EPTN Faults Detection network

After running hyperparameter refinement simulations, the most optimum finetune value was recorded and incorporated into each model to achieve the localisation and classification of the different EPTN component faults. Using these proposed models (SSD MobNet, SSD Rest101, and SSD Rest50), a four-class ETPN fault object detection was performed on our testing dataset containing 142 missing knobs, 75 broken insulators, 73 rusty clamps, and 45 missing insulator plate faults. The models were tested using three separate metrics, namely F_1-score and mAP. As previously mentioned in section 5.3, a holdout validation scheme is employed to produce an average detection result for all the utilized models in the study area. The precision rate, recall rate, and the average f_1 score explained in section 5.5 are used to measure the developed method's effectiveness on the testing dataset.

The test results of the proposed single-phase components' faults identification and classification pipeline are shown in Table 6.3. It illustrates the precision, recall, f1 score, and mAP of the three models, respectively. As can be seen from Table 6.3, the SSD ResNet holds the maximum mAP score of about 89.61% for the components' faults detected and classified. Low precision rates suggest that a significant number of false positive samples of the different EPTN component faults are generated when using the models for fault classification, which is not the case here as the model generated fewer false positive samples of EPTN faults; hence the reason for the general precision rate being above 90.90%. Alternatively, there are more component faults not identified than misclassified, causing a lower recall rate, especially for the missing knob fault type. The recall rate of the SSD Rest50 is 57.14%, 73.94%, and 83.56% for missing knob and rusty clamp fault classes, respectively, which varies about 15.50%, and 5.48% to that detected and classified by SSD Rest101.

Alternatively, the recall rate for the SSD Rest 101 is the greatest in identifying the broken and missing insulator faults. The SSD Rest50 achieved a better recall rate for broken insulator cap, missing insulator cap, missing knob, and rusty clamp component fault classes compared to SSD MobNet by 4.00%, 10.21%, 8.70%, and 4.11%. The SSD MobNet performs the least optimally in detecting and classifying the missing insulator fault class compared to that of the SSD Rest101 and SSD Rest50 models. Generally, all models had a satisfactory recall ability to detect and classify each fault class, especially for identifying missing knob and rusty clamp faults. This reveals that the experimental single-stage components' fault detection and classification pipeline can solve this identified problem by substantially increasing the model's performance in identifying and classifying the EPTN faults.

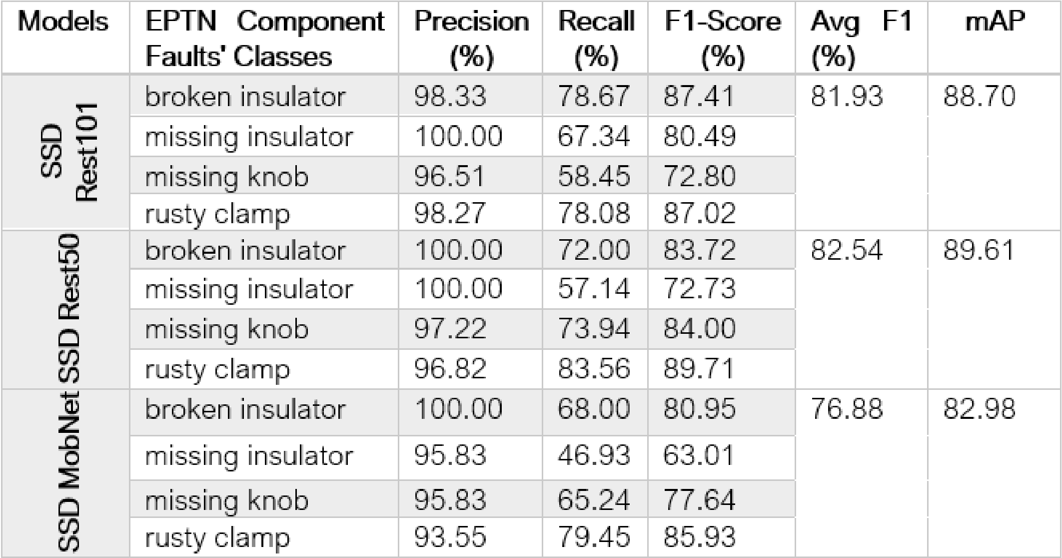

Models	EPTN Component Faults' Classes	Precision (%)	Recall (%)	F1-Score (%)	Avg F1 (%)	mAP
SSD Rest101	broken insulator	98.33	78.67	87.41	81.93	88.70
	missing insulator	100.00	67.34	80.49		
	missing knob	96.51	58.45	72.80		
	rusty clamp	98.27	78.08	87.02		
SSD Rest50	broken insulator	100.00	72.00	83.72	82.54	89.61
	missing insulator	100.00	57.14	72.73		
	missing knob	97.22	73.94	84.00		
	rusty clamp	96.82	83.56	89.71		
SSD MobNet	broken insulator	100.00	68.00	80.95	76.88	82.98
	missing insulator	95.83	46.93	63.01		
	missing knob	95.83	65.24	77.64		
	rusty clamp	93.55	79.45	85.93		

Table 6.3: Assessment of SSD Rest101, SSD Rest50, and SSD MobNet on the test dataset.

The SSD Rest101 is the second-best model with a mAP of 88.70%. Of the object detection methods tested, the one that delivered the least prediction (82.98%) was SSD MobNet. While the ResNet 101 derived model termed the SSD Rest101 is usually predicted to do the best in principle; however, in this case, the SSD model based on ResNet 50 contrasts conventional assumptions by revealing an improved result. The complexity of the network architecture can indeed justify the explanation behind the persistent lower results by ResNet 101 model, which is made of much deeper layers in contrast to the size of the training dataset; making the model characteristics over subsample and learns features; thus, affecting the performance of detecting the different components' faults optimally.

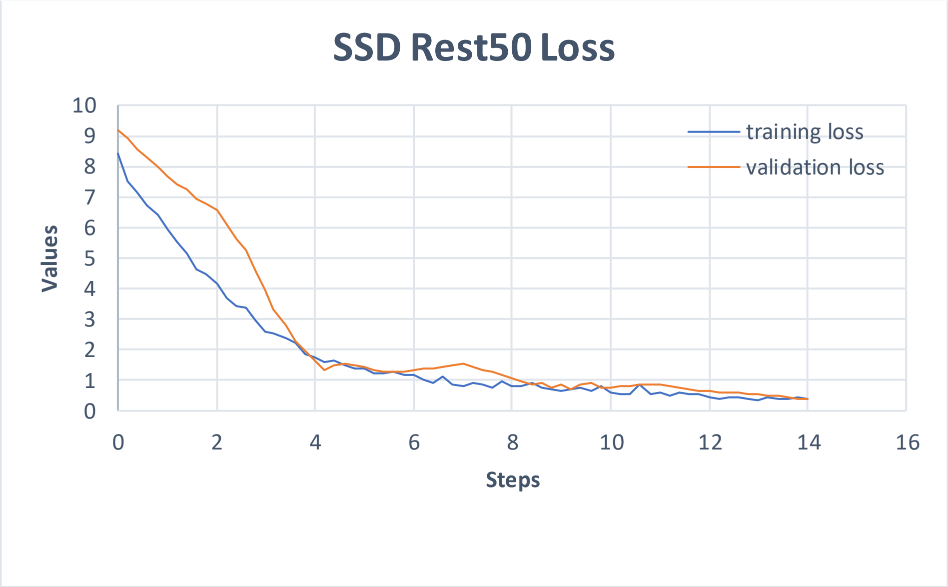

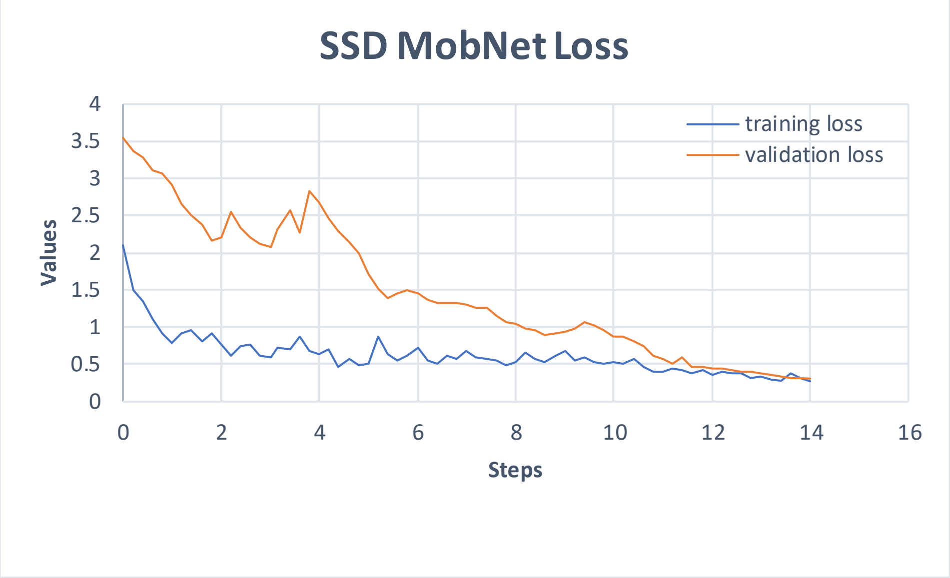

Figure 6.3: Epoch vs. Loss Graphs.

Furthermore, to intuitively reflect the proposed model's detection performance, the loss value graph was evaluated to understand, rationalize, and justify the proposed models' generalization ability. In general, we can assess the proposed model's performance using the loss graphs and the summary information of the validation loss and examine the group of classification, localisation, and regularization loss [57]. Figure 6.3 gives snapshots of the loss values sensitivity over the training and validation phase over the network trajectory. A good performance is established by a total and validation loss that reduces until it becomes stable and the difference between both loss values reaches a minimum [82]. If the prediction errors are unbiased, the validation error should be near zero, and the validation loss decrease with a decrease in training loss. This can be seen distinctively by the loss graph of SSD Rest50, SSD Rest101, and SSD MobNet model. The Rest50 model represents a Deep network; the SSD Rest 101 can be seen as a super Deep Network, while the SSD MobNet is a shallow network.

It can be seen that the various weight optimizations associated with the training and validation of the dataset based on the model architecture show that the loss value remained relatively stable. In the experiments, the base and top CNN layer used the Rectified Linear Units (ReLUs) [31] as activation functions over shuffled mini-batch gradient descent (batch size of 8) with the Adam optimization algorithm. The final output uses a sigmoid classifier for each decision node. Using the sigmoid activation, the final achieved pair total losses, i.e., [validation loss, training loss] for the SSD MobNet, SSD Rest50, and SSD Rest101, were approximately equal to [0.281, 0.309], [0.378, 0.385] and [0.356, 0.342] respectively.

In contrast to the SSD MobNet, SSD Rest50 and SSD Rest101 have higher orders of magnitude as they have more parameters because they have more layers and more filters per layer. This allowed the model to adapt to more convoluted representations (features) than the shallow network can provide. In the SSD Rest101, it is observable that the dataset was not sufficient to train the deeper network. The ResNet 50 backbone architecture, which represents the Deep Network, performs much better in minimizing the loss values than the other two networks, accomplishing train and validation losses of 0.378 and 0.385, respectively, after 15 epochs. Finally, there is a strong link between training loss and validation loss. They both decrease and then become stable at a constant value. This suggests that the model is correctly trained and has a high probability of working well over testing data within this domain.

6.3 Further Investigation

It should be noted that the proposed method and the SSMD [85] method achieve a high precision rate but have a lesser recall rate, especially for the missing insulator cap faults. This can be attributed to the inability to identify small-scale missing cap insulator location due to minuscule pixel area (about 20 x 20 pixel) indistinguishable from each other in the 600 × 600-pixel input patch image. After the downsampling of pooled CNN outputs, much of the semantic information about missing insulator cap fault would be overwritten by the contextual background. This will lead to difficulty in identifying faults, such as the missing insulator caps. Also, the lack of sufficient missing insulator samples in the test dataset could be responsible. However, this study's proposed method incorporates other component fault types all at once, which cannot be seen in the other developed model and could be somewhat said to be responsible for the low satisfactory recall rate. As far as these fault detection methods' overall efficiency is concerned, the proposed method has demonstrated that the algorithms' continued developments could be improved.

The proposed system performs object detection using a series of weights extracted from a set of representative random seeds, where each weight corresponds to a specific perspective of the problem being considered (four-component faults) and is developed using an iterative method in which alternative refining and integration of compatible training examples are performed. SSD has shown the capacity to detect multiclass faults from the UAV imagery; however, improvements such as image tiling to tackle small-scale problems and sufficient datasets are required. While experimenting with the model, overfit and exploding gradient sometimes manifest, which can be resolved by different techniques, requiring training the model over long periods. Finally, our findings show much greater precision using well-calibrated UAV images and a reasonably good recall rate. In summary, the comparison with detection results from the literature review with the analysis in this current work indicates the suitability of deep learning to monitor and detect components fault on electric power transmission networks to help the decision-making process required for asset management in developing countries like Nigeria.

6.4 Qualitative Experimental Evaluations

Figure 6.4 provides an example of all the output images produced by all the models implemented. The sky-blue box denotes the missing insulator; the green box denotes the broken insulator, the turquoise box denotes the missing knob faults, while the white box bounds the rusty clamp defects. Each box is marked by the components' faults and its confidence score. In contrast, the red ellipse show faults undetected by the models. The first column to the third column depicts the implemented method's performance, SSD MobNet, SSD Rest101, and SSD Rest50, respectively.

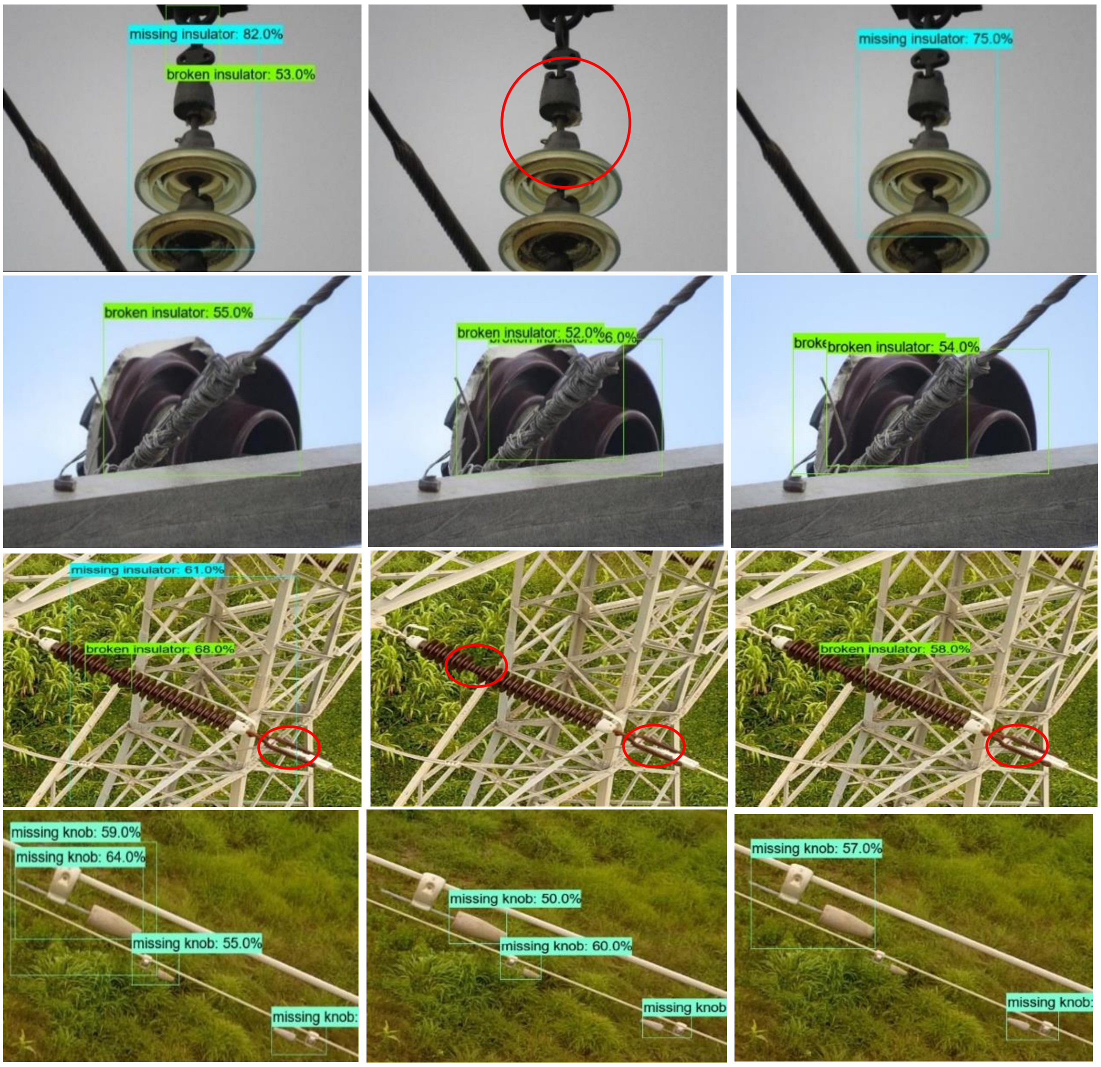

Figure 6.4: Experimental results of the four components faults. The first column to the third column depicts the proposed method's performance in each row, SSD MobNet, SSD Rest50, and SSD Rest101.

In the first row, the SSD MobNet (leftmost) gives an accurate detection of the missing insulator plate with a false positive identification of broken insulator, SSD Rest101 (middle) gives no result even with the presence of missing insulator plate and the SSD Rest50 (rightmost) achieves the best result with no false prediction. In the second row of Figure 6.4, the SSD Rest50 method detects the broken insulator fault, while the other implemented model leads to a wrong judgment with a false rate. In the third row, the model's performance behaves similarly to what is observed in the first row as the model is affected by the convoluted background interferences. The fourth row shows that all the implemented models had depicted the missing knob near perfectly with just one false positive of the missing knob faults for SSD MobNet (leftmost) and one false negative (rightmost).

7 Conclusion

7.1 Findings

This thesis explores the use of high-resolution multispectral UAV-based imagery for electric power transmission line component fault detection using the deep learning approach without any physical participation by the site inspection by engineers. This research's feasibility test was conducted using the Shiroro-Kaduna transmission network in Niger State as a case study, one of the substations for the Transmission Company of Nigeria. The results demonstrate the feasibility of using high-resolution multispectral UAV-based imagery to identify and classify transmission component faults, particularly for emerging and formative transmission companies in developing countries confronted by data scarcity, asset seclusion, and insecurity ground-surveys complexity, untimeliness, and general human cost. The final models utilizing SSD object detection pipeline were developed in this study as an approach for power transmission network components fault identification. After analysing the results of the revealed studies, some important conclusions can be reached, such as:

a) *Which are different hyperparameters finetuning yields the best results in the implemented deep learning model?*

To help address this research query, all the chosen object detection models using various backbone architecture were implemented in Chapter 5[3]. The models' efficiency was analysed in an exhaustive hyperparameter configuration setting to choose the best hyperparameter values. In addition to this, some retrospective studies were run to assess the usefulness of the DCNN. The following conclusions were observed:

- Transfer learning is a better strategy to follow to produce short-term outcomes. Since the issue being discussed requires data that is not identical to current datasets (weights trained on images with little or no geocentric interests), processing just the weights of the pre-trained model resulted in a more robust outcome than freezing the layers, with the repercussion of a slower training method. This helps scopes out the model weight so that the model weight optimization is not starting from scratch, i.e., net-zero but from an existing optimal value for each convolution layer;
- The adaptive optimizer, momentum with mini-batch SGD, allowed for the faster convergence of the proposed model and to automatically predict the optimum learning rate;
- It was observed that higher learning rate achieved better mAP values across all the models implemented;

---

[3] The source code of this implementation can be found at: https://github.com/EmekaKing/Felect

- During preparation, the objects' measurements in the images were precisely calculated to determine the best values for the anchor parameters accurately. The model achieved better mAP by using the default three aspect ratio value.
- Furthermore, data augmentation was a vital technique allowing the model to manage invariance among the component fault classes and improve the size of a training dataset.

b) *To what extent will the deep convolution neural network perform based on the predicted component fault classes' performance metrics analysis?*

The assessment of object detection models showed that the implemented SSD selected based on speed and computing capabilities models achieve excellent results both in localising and classifying components faults utilizes high-resolution RGB images with complex background context. The deep learning object detection models implemented offered high mAP, with SSD Rest50 achieving the best, followed by SSD Rest101 and SSD MobNet regarding mAP and F_1-score. Given the findings, we can deduce that in the case of related network architectures, SSD Rest50 performs better than SSD Rest101, demonstrating that spatial and semantic knowledge and representations with the right proportion of deep layers like SSD Rest50 obtains a better detection accuracy. Second, the improved performance of ConvNet SSD MobNet indicates that the least-complex network architecture with the lesser number of filters does not lead to increased accuracy of the model and that any smaller native model with fewer blocks could require a much deeper or broader design. In the final step, the applied models' competence was checked by the final achieved error based on the loss values deducted by the difference between the training error and validation error. The final model shows that our EPTN fault detection accuracy is feasible and achievable with remarkable performance.

With this, the thesis's aim was achieved, which is "*to propagate the possibility of detecting and inspecting EPTN assets of Electric Utilities in Nigeria utilizing UAV imagery and deep learning approach.*" In summary, the findings are positive and optimistic. It can be seen that object detection strategies could help monitor faults on transmission lines, monitor assets, and optimize EPTN for Transmission companies using deep learning. Further research on applying other deep neural networks, i.e., instance segmentation model to different transmission line components fault identification, is encouraged.

7.2 Limitation

While the study produced promising research findings, there are several limitations and opportunities for further research, mainly dataset sampling, and standardized evaluation metrics. A majority of EPTN corridors use a wide variety of power line components. Consequently, the grids are exposed to a tremendous range of problems. Additionally, other small defects in power line components such as missing knobs and rust can occur in various forms and simultaneously; and are described differently based on the expertise and technical framework of electric utilities. This, combined with the lack of uniform training/validation data, presents a significant challenge for the inspection of vision-based faults using a combination of RGB imagery and DL due to the lack of templates for classifying unknown groups.

Regarding the evaluation baseline, the assessment of object detection projects is subjective. There is little standard exposition in studies concerning analysis metrics and computation, especially against the dataset, and the degree to which the analysis methods generalize are still limited. The final output containing a bounding box should undergo digital photogrammetry workflow to form a 3D electrical transmission model network and further analyzed to identify severity level to assist site inspectors and engineers in planning and implementing fault repairs across multiple remote and unsecured locations. Due to image acquisition technical specifications limitations and some deficient computer science skills, concrete cartographic products (maps) are not provided. Hence, the result contained a CSV file containing the bounding box's coordinates, fault type, and confidence sore, and the detected tiled images with bounding box overlaid and linked to the original geolocated imagery. Consequently, investigating spatial patterns existing among the fault detected fell outside this thesis's scope.

7.3 Future Works

The findings discussed in Chapter 6 have several aspects that require further analysis. To enhance this analysis, several possible steps are posited:

First, the single-stage component identification and classification pipeline should be expanded to account for faults in different components' shapes and severity levels. Two phases are used simultaneously in the developed frameworks: first, location of components faults; second, determination and classification of the component faults. The pipeline can detect four different types of defects from inspection images; however, it cannot measure the magnitude of the detected defects' scale. One alternative solution is to determine the limits of the observed faults directly at the precise pixel level by applying instance segmentation and uses this knowledge to measure the scale and magnitude of the faults by, for example, estimating the defect/component pixel ratio.

Second, this study concentrates on only high-resolution multispectral RGB (visible) bands of the electric transmission network corridor right-of-way (ROW). Hence there is a need to incorporate other various data sources that adopt the other electromagnetic channel such as thermal images, ultraviolet images, aerial and mobile laser scanning images. This will allow creating a model pipeline inclusive to others not detectable by the human eye, such as wire failure and corona discharges.

Third, power transmission networks have various components, and issues arise in different positions concerning these components. These components have several different instances and manifestations, and those instances can have different characteristics such as colour, form, texture, scale, and content. Furthermore, the change in imaging state will result in the object's presence being affected consistently. The dynamic context involves the photo's direction and distance, occlusion, context, and lighting conditions. Two methods can be explored to solve the issue of component fault imbalance and intra-component variation. They include foreground and background overlay using segmentation network and image processing technique; and Generative Adversarial Networks (GANs) to create synthetic images.

Fourth, the model can be extended to cover for real-time autonomous vision detection in the field incorporated with GPS-INS navigation, i.e., motion pictures. This can be consolidated into synchronized database logging camera GPS position and time logs and linked to a multiple object monitoring algorithm to allow fully automated asset management during data acquisition.

Bibliographic References

[1] S. Alkire, A. Conconi, G. Robles, and A. V. June, “Who and where are the poorest of the poor?” 2015.

[2] R. B. Johnston, “Arsenic and the 2030 Agenda for sustainable development,” *Arsen. Res. Glob. Sustain. - Proc. 6th Int. Congr. Arsen. Environ. AS 2016*, pp. 12–14, 2016, doi: 10.1201/b20466-7.

[3] L. Matikainen *et al.*, “Remote sensing methods for power line corridor surveys,” *ISPRS J. Photogramm. Remote Sens.*, vol. 119, pp. 10–31, 2016, doi: 10.1016/j.isprsjprs.2016.04.011.

[4] D. Mentis *et al.*, “Energy for Sustainable Development A GIS-based approach for electrification planning — A case study on Nigeria,” *Energy Sustain. Dev.*, vol. 29, pp. 142–150, 2015, doi: 10.1016/j.esd.2015.09.007.

[5] P. Bertheau, C. Cader, and P. Blechinger, “Electrification modelling for Nigeria,” *Energy Procedia*, vol. 93, no. March, pp. 108–112, 2016, doi: 10.1016/j.egypro.2016.07.157.

[6] B. Meehan, *Modelling Electricity Distribution with GIS*, 1st Editio. ESRI Press, 2013.

[7] Ikeja Electric (IE), “Sustainability Report,” Lagos, 2016.

[8] P. Mayer and P. Mayer, “Corrosion evaluation methods for power transmission lines.”

[9] Matergenics, “Corrosion Inspection of Power Transmission Structures,” 2020. http://www.matergenics.com/drone-inspection-services/corrosion-inspection-of-power-transmission-structures (accessed May 15, 2020).

[10] H. Baorong, *The Cost of Corrosion in China*, 1st Ed. Netherlands: Beijing: Science Press/ Springer, 2019.

[11] Y. Hu and K. Liu, *Remote sensing and remote measurement technology of transmission lines*. 2017.

[12] H. Guan, Y. Yu, J. Li, Z. Ji, and Q. Zhang, “Extraction of power-transmission lines from vehicle-borne lidar data,” *Int. J. Remote Sens.*, vol. 37, no. 1, pp. 229–247, 2016, doi: 10.1080/01431161.2015.1125549.

[13] A. Zormpas, K. Moirogiorgou, K. Kalaitzakis, G. A. Plokamakis, and P. Partsinevelos, “Power Transmission Lines Inspection using Properly Equipped Unmanned Aerial Vehicle (UAV),” *2018 IEEE Int. Conf. Imaging Syst. Tech.*, pp. 1–5, 2018.

[14] J. Ahmad, A. S. Malik, M. F. Abdullah, N. Kamel, and L. Xia, “A novel method for

vegetation encroachment monitoring of transmission lines using a single 2D camera," *Pattern Anal. Appl.*, vol. 18, no. 2, pp. 419–440, 2015, doi: 10.1007/s10044-014-0391-9.

[15] X. Yu, X. Wu, C. Luo, and P. Ren, "Deep learning in remote sensing scene classification: a data augmentation enhanced convolutional neural network framework," *GIScience Remote Sens.*, vol. 54, no. 5, pp. 741–758, 2017, doi: 10.1080/15481603.2017.1323377.

[16] Y. Baştanlar and M. Özuysal, "Introduction to machine learning," *Methods Mol. Biol.*, vol. 1107, pp. 105–128, 2014, doi: 10.1007/978-1-62703-748-8_7.

[17] R. A. McLaughlin, "Extracting transmission lines from airborne LIDAR data," *IEEE Geosci. Remote Sens. Lett.*, vol. 3, no. 2, pp. 222–226, 2006, doi: 10.1109/LGRS.2005.863390.

[18] Y. Hu and K. Liu, *Parameters and characteristics of transmission lines*. 2017.

[19] G. E. Braga and R. M. R. Junqueira, "Methodology for Planning Tower Leg Foundations Corrosion Maintenance of Overhead Transmission Lines Based on GIS," *IEEE Trans. Power Deliv.*, vol. 31, no. 4, pp. 1601–1608, 2016, doi: 10.1109/TPWRD.2016.2524003.

[20] Z. Lin, Z. Xu, and I. Engineering, "A METEOROLOGICAL RISK ASSESSMENT METHOD FOR POWER LINES BASED," vol. III, no. July, pp. 12–19, 2016, doi: 10.5194/isprsannals-III-8-19-2016.

[21] K. Chen, C. Huang, and J. He, "Fault detection, classification and location for transmission lines and distribution systems: A review on the methods," *High Volt.*, vol. 1, no. 1, pp. 25–33, 2016, doi: 10.1049/hve.2016.0005.

[22] V. C. Ogboh and T. C. Madueme, "Investigation of Faults on the Nigerian Power System Transmission Line Using Artificial Neural Network," *Int. J. Res. Manag. Sci. Technol. (E*, vol. 3, no. 4, pp. 87–95, 2015, [Online]. Available: www.ijrmst.org.

[23] F. Miralles, N. Pouliot, and S. Montambault, "State-of-the-art review of computer vision for the management of power transmission lines," *Proc. 3rd Int. Conf. Appl. Robot. Power Ind. CARPI 2014*, 2015, doi: 10.1109/CARPI.2014.7030068.

[24] Z. A. Siddiqui and U. Park, "A Drone Based Transmission Line Components Inspection System with Deep Learning Technique," *Energies*, vol. 13, no. 13, pp. 1–24, 2020, doi: 10.3390/en13133348.

[25] Z. Zhao, G. Xu, Y. Qi, N. Liu, and T. Zhang, "Multi-patch deep features for power line insulator status classification from aerial images," *Proc. Int. Jt. Conf. Neural Networks*, vol. 2016-October, pp. 3187–3194, 2016, doi: 10.1109/IJCNN.2016.7727606.

[26] Y. Wang and B. Yan, "Vision-based detection and location for cracked insulator," *Comput. Eng. Des.*, vol. 35, no. 2, pp. 583–587, 2014, [Online]. Available:

https://pay.cnki.net/zscsdoc/download?flag=cnkispace&plat=cnkispace&filename=SJSJ201402043&dbtype=CJFD&year=2014&dtype=pdf.

[27] Z. Xue, S. Luo, Y. Chen, and L. Tong, "The application of the landslides detection method based on SAR images to transmission line corridor area," *2016 13th Int. Comput. Conf. Wavelet Act. Media Technol. Inf. Process. ICCWAMTIP 2017*, pp. 163–166, 2017, doi: 10.1109/ICCWAMTIP.2016.8079829.

[28] L. Yan, W. Wu, and T. Li, "Power transmission tower monitoring technology based on TerraSAR-X products," *Int. Symp. Lidar Radar Mapp. 2011 Technol. Appl.*, vol. 8286, p. 82861E, 2011, doi: 10.1117/12.912336.

[29] S. Li *et al.*, "Study on extra-high voltage power line scatterers in time series SAR," *3rd Int. Work. Earth Obs. Remote Sens. Appl. EORSA 2014 - Proc.*, no. May 2016, pp. 47–51, 2014, doi: 10.1109/EORSA.2014.6927847.

[30] Y. Liu, K. Xu, S. Shi, and T. Li, "Effects of Span Length and Radar Polarimetry on the Backscattering Characteristics of Ultra-High Voltage Power Transmission Line in TerraSAR-X Images," *5th Int. Work. Earth Obs. Remote Sens. Appl. EORSA 2018 - Proc.*, pp. 5–9, 2018, doi: 10.1109/EORSA.2018.8598570.

[31] J. Ahmad, A. S. Malik, L. Xia, and N. Ashikin, "Vegetation encroachment monitoring for transmission lines right-of-ways: A survey," *Electr. Power Syst. Res.*, vol. 95, pp. 339–352, 2013, doi: 10.1016/j.epsr.2012.07.015.

[32] X. Yu *et al.*, "Comparison of laser and stereo optical, SAR and InSAR point clouds from the air- and space-borne sources in the retrieval of forest inventory attributes," *Remote Sens.*, vol. 7, no. 12, pp. 15933–15954, 2015, doi: 10.3390/rs71215809.

[33] M. Jaya Bharata Reddy, B. Karthik Chandra, and D. K. Mohanta, "Condition monitoring of 11 kV distribution system insulators incorporating complex imagery using combined DOST-SVM approach," *IEEE Trans. Dielectr. Electr. Insul.*, vol. 20, no. 2, pp. 664–674, 2013, doi: 10.1109/TDEI.2013.6508770.

[34] J. Jiang, L. Zhao, J. Wang, Y. Liu, M. Tang, and Z. Ji, "The electrified insulator parameter measurement for flashover based on photogrammetric method," *MIPPR 2011 Multispectral Image Acquis. Process. Anal.*, vol. 8002, no. 86, p. 80021I, 2011, doi: 10.1117/12.902054.

[35] R. V. Ussyshkin, L. Theriault, M. Sitar, and T. Kou, "Advantages of airborne lidar technology in power line asset management," *2011 Int. Work. Multi-Platform/Multi-Sensor Remote Sens. Mapping, M2RSM 2011*, pp. 1–5, 2011, doi: 10.1109/M2RSM.2011.5697427.

[36] L. F. Luque-Vega, B. Castillo-Toledo, A. Loukianov, and L. E. Gonzalez-Jimenez, "Power line inspection via an unmanned aerial system based on the quadrotor helicopter," *Proc. Mediterr. Electrotech. Conf. - MELECON*, no. April, pp. 393–397, 2014, doi: 10.1109/MELCON.2014.6820566.

[37] M. Wang, W. Tong, and S. Liu, "Fault detection for power line based on

convolution neural network," *ACM Int. Conf. Proceeding Ser.*, vol. Part F128535, pp. 95–101, 2017, doi: 10.1145/3094243.3094254.

[38] Y. Tiantian, Y. Guodong, and Y. Junzhi, "Feature fusion-based insulator detection for aerial inspection," *Chinese Control Conf. CCC*, pp. 10972–10977, 2017, doi: 10.23919/ChiCC.2017.8029108.

[39] K. Chen, J. Hu, and J. He, "Detection and Classification of Transmission Line Faults Based on Unsupervised Feature Learning and Convolutional Sparse Autoencoder," *IEEE Trans. Smart Grid*, vol. 9, no. 3, pp. 1748–1758, 2018, doi: 10.1109/TSG.2016.2598881.

[40] Y. Song *et al.*, "A vision-based method for the broken spacer detection," *2015 IEEE Int. Conf. Cyber Technol. Autom. Control Intell. Syst. IEEE-CYBER 2015*, pp. 715–719, 2015, doi: 10.1109/CYBER.2015.7288029.

[41] Y. Hao *et al.*, "Icing condition assessment of in-service glass insulators based on graphical shed spacing and graphical shed overhang," *Energies*, vol. 11, no. 2, 2018, doi: 10.3390/en11020318.

[42] L. Yang *et al.*, "Recognition of natural ice types on in-service glass insulators based on texture feature descriptor," *IEEE Trans. Dielectr. Electr. Insul.*, vol. 24, no. 1, pp. 535–542, 2017, doi: 10.1109/TDEI.2016.006049.

[43] Y. Zhai, H. Cheng, R. Chen, Q. Yang, and X. Li, "Multi-saliency aggregation-based approach for insulator flashover fault detection using aerial images," *Energies*, vol. 11, no. 2, pp. 1–12, 2018, doi: 10.3390/en11020340.

[44] Y. Zhai, D. Wang, M. Zhang, J. Wang, and F. Guo, "Fault detection of insulator based on saliency and adaptive morphology," *Multimed. Tools Appl.*, vol. 76, no. 9, pp. 12051–12064, 2017, doi: 10.1007/s11042-016-3981-2.

[45] J. Han *et al.*, "A method of insulator faults detection in aerial images for high-voltage transmission lines inspection," *Appl. Sci.*, vol. 9, no. 10, pp. 1–22, 2019, doi: 10.3390/app9102009.

[46] J. Han *et al.*, "Search like an eagle: A cascaded model for insulator missing faults detection in aerial images," *Energies*, vol. 13, no. 3, pp. 1–20, 2020, doi: 10.3390/en13030713.

[47] X. Li, N. Kwok, J. E. Guivant, K. Narula, R. Li, and H. Wu, "Detection of imaged objects with estimated scales," *VISIGRAPP 2019 - Proc. 14th Int. Jt. Conf. Comput. Vision, Imaging Comput. Graph. Theory Appl.*, vol. 5, no. October, pp. 39–47, 2019, doi: 10.5220/0007353600390047.

[48] J. Fu, G. Shao, L. Wu, L. Liu, and Z. Ji, "Defect detection of line facility using a hierarchical model with a learning algorithm," *High Volt. Eng. Dep. CEPRI*, vol. 43, no. 1, pp. 266–275, 2017, doi: 10.13336/j.1003-6520.hve.20161227035.

[49] T. Mao *et al.*, "Defect recognition method based on HOG and SVM for drone inspection images of the power transmission line," *2019 Int. Conf. High Perform.*

Big Data Intell. Syst. HPBD IS 2019, no. 61701404, pp. 254–257, 2019, doi: 10.1109/HPBDIS.2019.8735466.

[50] Y. Liu *et al.*, “2016 4th International Conference on Applied Robotics for the Power Industry, CARPI 2016,” *2016 4th Int. Conf. Appl. Robot. Power Ind. CARPI 2016*, pp. 1–5, 2016.

[51] X. Hui, J. Bian, X. Zhao, and M. Tan, “Vision-based autonomous navigation approach for unmanned aerial vehicle transmission-line inspection,” *Int. J. Adv. Robot. Syst.*, vol. 15, no. 1, pp. 1–15, 2018, doi: 10.1177/1729881417752821.

[52] L. Ma, C. Xu, G. Zuo, B. Bo, and F. Tao, “Detection Method of Insulator Based on Faster R-CNN,” *2017 IEEE 7th Annu. Int. Conf. CYBER Technol. Autom. Control. Intell. Syst. CYBER 2017*, pp. 1410–1414, 2018, doi: 10.1109/CYBER.2017.8446155.

[53] X. Liu, H. Jiang, J. Chen, J. Chen, S. Zhuang, and X. Miao, “Insulator Detection in Aerial Images Based on Faster Regions with Convolutional Neural Network,” *IEEE Int. Conf. Control Autom. ICCA*, vol. 2018-June, pp. 1082–1086, 2018, doi: 10.1109/ICCA.2018.8444172.

[54] P. Soviany and R. T. Ionescu, “Optimizing the trade-off between single-stage and two-stage deep object detectors using image difficulty prediction,” *Proc. - 2018 20th Int. Symp. Symb. Numer. Algorithms Sci. Comput. SYNASC 2018*, pp. 209–214, 2018, doi: 10.1109/SYNASC.2018.00041.

[55] E. Hanna and M. Cardillo, “Faster R-CNN2015,” *Biol. Conserv.*, vol. 158, pp. 196–204, 2013.

[56] R. F. C. Networks and J. Dai, “Aron cap II - A crítica filosófica.pdf.”

[57] W. Liu *et al.*, “SSD Net,” *Lect. Notes Comput. Sci. (including Subser. Lect. Notes Artif. Intell. Lect. Notes Bioinformatics)*, vol. 9905 LNCS, pp. 21–37, 2015.

[58] Y. Yang, L. Wang, Y. Wang, and X. Mei, “Insulator self-shattering detection: a deep convolutional neural network approach,” *Multimed. Tools Appl.*, vol. 78, no. 8, pp. 10097–10112, 2019, doi: 10.1007/s11042-018-6610-4.

[59] X. Tao, D. Zhang, Z. Wang, X. Liu, H. Zhang, and D. Xu, “Detection of power line insulator defects using aerial images analyzed with convolutional neural networks,” *IEEE Trans. Syst. Man, Cybern. Syst.*, vol. 50, no. 4, pp. 1486–1498, 2020, doi: 10.1109/TSMC.2018.2871750.

[60] R. Bai, H. Cao, Y. Yu, F. Wang, W. Dang, and Z. Chu, “Insulator Fault Recognition Based on Spatial Pyramid Pooling Networks with Transfer Learning (Match 2018),” *ICARM 2018 - 2018 3rd Int. Conf. Adv. Robot. Mechatronics*, pp. 824–828, 2019, doi: 10.1109/ICARM.2018.8610720.

[61] J. Brownlee, “Crash Course in Convolutional Neural Networks for Machine Learning,” *Machine Learning Mastery*, 2019. https://machinelearningmastery.com/crash-course-convolutional-neural-

networks/ (accessed Oct. 23, 2020).

[62] C. Francois, *Deep Learning with Python*, vol. 53, no. 9. 2019.

[63] K. O'Shea and R. Nash, "An Introduction to Convolutional Neural Networks," pp. 1–11, 2015, [Online]. Available: http://arxiv.org/abs/1511.08458.

[64] D. of C. S. U. Stanford, "CS231n: Convolutional Neural Networks for Visual Recognition," *STANFORD VISION AND LEARNING LAB*. https://cs231n.github.io/convolutional-networks/ (accessed Nov. 21, 2020).

[65] R. Shanmugamani, A. G. A. Rahman, S. M. Moore, and N. Koganti, *Deep Learning for Computer Vision: Expert techniques to train advanced neural networks using Tensorflow and Keras.*, 1st ed. Birmingham, UK: Packt Publishing Ltd, 2018.

[66] H. Li, Z. Xu, G. Taylor, C. Studer, and T. Goldstein, "Visualizing the loss landscape of neural nets," *arXiv*, vol. 1, no. NeurIPS 2018, pp. 1–11, 2017.

[67] S. Saha, "A Comprehensive Guide to Convolutional Neural Networks — the ELI5 way," *Medium*, 2018. https://towardsdatascience.com/a-comprehensive-guide-to-convolutional-neural-networks-the-eli5-way-3bd2b1164a53 (accessed Nov. 15, 2020).

[68] L. Pasteur and R. Koch, "Gradient-Based Learning Methods," vol. 74, no. 1934, pp. 535–546, 1941.

[69] A. Géron, *Hands-on machine learning with Scikit-Learn and TensorFlow: concepts, tools, and techniques to build intelligent systems.*, 2nd Editio. California, United States of America: O'Reilly Media, Inc., 2019.

[70] Y. Zhang, J. Gao, and H. Zhou, "Breeds Classification with Deep Convolutional Neural Network," *ACM Int. Conf. Proceeding Ser.*, pp. 145–151, 2020, DOI: 10.1145/3383972.3383975.

[71] A. G. Howard and W. Wang, "MobileNets: Efficient Convolutional Neural Networks for Mobile Vision Applications," 2012. arXiv:1704.04861v1.

[72] J. W. Yun, "Deep Residual Learning for Image Recognition arXiv:1512.03385v1," *Enzyme Microb. Technol.*, vol. 19, no. 2, pp. 107–117, 2015, [Online]. Available: https://arxiv.org/pdf/1512.03385.pdf.

[73] A. Rosebrock, "ImageNet: VGGNet, ResNet, Inception, and Xception with Keras," *pyimagesearch*, 2017. https://www.pyimagesearch.com/2017/03/20/imagenet-vggnet-resnet-inception-xception-keras/ (accessed Nov. 25, 2020).

[74] J. Huang *et al.*, "Speed/accuracy trade-offs for modern convolutional object detectors," *Proc. - 30th IEEE Conf. Comput. Vis. Pattern Recognition, CVPR 2017*, vol. 2017-January, pp. 3296–3305, 2017, doi: 10.1109/CVPR.2017.351.

[75] Y. Konishi, Y. Hanzawa, M. Kawade, and M. Hashimoto, "Fast 6D Pose Estimation Using Hierarchical Pose Trees," *Eccv*, vol. 1, pp. 398–413, 2016, DOI:

10.1007/978-3-319-46448-0.

[76] W. Shi, S. Bao, and D. Tan, “FFESSD: An accurate and efficient single-shot detector for target detection,” *Appl. Sci.*, vol. 9, no. 20, 2019, doi: 10.3390/app9204276.

[77] T. Olawale and S. A. Ad, “REPORT ON Student Industrial Work Experience Scheme (SIWES) AT Transmission Company of Nigeria (TCN) for the Student Industrial Work Experience Scheme (SIWES),” no. August 2018, 2018, doi: 10.13140/RG.2.2.35067.05929.

[78] JICA Study Team & TCN, “CHAPTER 7 Transmission Network Development Plan,” 2020.

[79] O. M. Komolafe and K. M. Udofia, “Review of electrical energy losses in Nigeria,” *Niger. J. Technol.*, vol. 39, no. 1, pp. 246–254, 2020, doi: 10.4314/njt.v39i1.28.

[80] M. P. Blimpo and M. Cosgrove-Davies, *Electricity Access in Sub-Saharan Africa: Uptake, Reliability, and Complementary Factors for Economic Impact*. 2019.

[81] S. Ioffe and C. Szegedy, “Batch normalization: Accelerating deep network training by reducing internal covariate shift,” *32nd Int. Conf. Mach. Learn. ICML 2015*, vol. 1, pp. 448–456, 2015.

[82] G. Perin and S. Picek, “On the Influence of Optimizers in Deep Learning-based Side-channel Analysis,” *Cryptol. ePrint Arch.*, no. Report 2020/977, pp. 1–22, 2020, [Online]. Available: https://eprint.iacr.org/2020/977.

[83] G. Cheng, J. Han, P. Zhou, and L. Guo, “Multi-class geospatial object detection and geographic image classification based on the collection of part detectors,” *ISPRS J. Photogramm. Remote Sens.*, vol. 98, pp. 119–132, 2014, doi: 10.1016/j.isprsjprs.2014.10.002.

[84] R. Padilla, “Object Detection Metrics.” 2018, [Online]. Available: https://github.com/rafaelpadilla/Object-Detection-Metrics.

[85] Z. Ling *et al.*, “An Accurate and Real-time Self-blast Glass Insulator Location Method Based On Faster R-CNN and U-net with Aerial Images,” *IEEE Geosci. Remote Sens. Lett.*, Jan. 2018, [Online]. Available: http://arxiv.org/abs/1801.05143.

[86] H. Alaskar, “Convolutional Neural Network Application in Biomedical Signals,” J. Comput. Sci. Inf. Technol., vol. 6, no. 2, pp. 45–59, 2018, doi: 10.15640/jcsit.v6n2a5.

Masters
Program
in **Geospatial**
Technologies

Supported by:
Education and Culture
ERASMUS MUNDUS